

**TITLE: Optical mapping of cAMP signaling at the nanometer scale**

**AUTHORS:** Andreas Bock<sup>1,2,7,\*</sup>, Paolo Annibale<sup>1,2,7</sup>, Charlotte Konrad<sup>1,2</sup>, Annette Hannawacker<sup>2</sup>, Selma E. Anton<sup>1,2</sup>, Isabella Maiellaro<sup>2</sup>, Ulrike Zabel<sup>2</sup>, Sivaraj Sivaramakrishnan<sup>3</sup>, Martin Falcke<sup>1,4</sup>, and Martin J. Lohse<sup>1,2,5,6,8,\*</sup>.

**AFFILIATIONS:**

<sup>1</sup>Max Delbrück Center for Molecular Medicine in the Helmholtz Association, Robert-Rössle-Str. 10, 13125 Berlin, Germany.

<sup>2</sup>Institute of Pharmacology and Toxicology, University of Würzburg, Versbacher Str. 9, 97078 Würzburg, Germany.

<sup>3</sup>Department of Genetics, Cell Biology, and Development, University of Minnesota, Minneapolis, Minnesota 55455, USA.

<sup>4</sup>Department of Physics, Humboldt University, Newtonstr. 15, 12489 Berlin, Germany.

<sup>5</sup>Institute for Chemistry and Biochemistry, Free University, Takustr. 3, 14195 Berlin

<sup>6</sup>ISAR Bioscience Institute, 82152 Munich/Planegg, Germany.

<sup>7</sup>These authors contributed equally

<sup>8</sup>Lead contact: Martin J. Lohse, [m.lohse@mdc-berlin.de](mailto:m.lohse@mdc-berlin.de)

\*Correspondence to: [andreas.bock@mdc-berlin.de](mailto:andreas.bock@mdc-berlin.de) (A.B.), [m.lohse@mdc-berlin.de](mailto:m.lohse@mdc-berlin.de) (M.J.L.; lead contact)

## SUMMARY:

Cells relay a plethora of extracellular signals to specific cellular responses using only a few *second messengers*, such as cAMP. To explain signaling specificity, cAMP-degrading phosphodiesterases (PDEs) have been suggested to confine cAMP to distinct cellular compartments. However, measured rates of fast cAMP-diffusion and slow PDE-activity render cAMP compartmentalization essentially impossible. Using fluorescence spectroscopy, we show that – contrary to earlier data – cAMP at physiological concentrations is predominantly bound to cAMP binding sites and, thus, immobile. Binding and unbinding results in largely reduced cAMP dynamics which we term '*buffered diffusion*'. With a large fraction of cAMP being buffered, PDEs can create nanometer-sized domains of low cAMP concentrations. Using FRET-cAMP nanorulers we directly map cAMP gradients at the nanoscale around PDE molecules and the areas of resulting downstream activation of cAMP-dependent protein kinase (PKA). Our study reveals that spatiotemporal cAMP signaling is under precise control of nanometer-sized domains shaped by PDEs that gate the activation of downstream effectors.

## INTRODUCTION:

Hundreds of cell surface receptors, notably G protein-coupled receptors (GPCRs), signal via the second messenger cyclic adenosine 3',5'-monophosphate (cAMP) and its effector proteins, in particular protein kinase A (PKA). This pathway is central to key physiological functions and, hence, also to many diseases, making it a highly attractive therapeutic target (Nikolaev et al., 2010, Gold et al., 2013, Zaccolo, 2009, Zaccolo, 2011, Perera and Nikolaev, 2013). However, it is unclear, how the huge number of receptors that all change global cellular cAMP levels can result in specific cellular responses. To explain receptor-specific responses observed in experiments and how these responses may differ in different regions of a cell, many researchers have proposed cAMP compartmentalization (Brunton et al., 1979, Hayes et al., 1980, Buxton and Brunton, 1983). The cAMP-degrading phosphodiesterases (PDEs) have been proposed to play a crucial role in establishing the cAMP gradients that are necessary to create such compartments (Houslay, 2010, Terrin et al., 2006, Mika et al., 2012, Stangherlin and Zaccolo, 2012).

However, several studies have determined that cAMP is highly diffusible in intact cells (Bacskai et al., 1993, Nikolaev et al., 2004, Chen et al., 1999, Nikolaev et al., 2006, Richards et al., 2016, Agarwal et al., 2016, Huang and Gillette, 1993) and **Table S1**), and PDEs have low catalytic rates (Omori and Kotera, 2007, Conti and Beavo, 2007, Bender and Beavo, 2006). Therefore, cAMP should very rapidly equilibrate in a cell (Rich et al., 2000, Rich et al., 2001, Feinstein et al., 2012, Lohse et al., 2017, Xin et al., 2015), and this would prevent the existence of compartments with different concentrations of cAMP. Thus, the important question whether and how intracellular cAMP might be compartmentalized has remained unresolved for decades.

We therefore set out to address this controversy by developing tools and methods to directly measure and characterize cAMP mobility in intact cells and at physiological levels, and to measure cAMP levels and gradients in real-time and with a spatial accuracy in the nanometer range.

## RESULTS:

### cAMP buffering restricts cAMP dynamics in intact cells

In order to visualize how signaling by cAMP is patterned, we aimed to develop and use new technologies that allow an analysis of cAMP diffusion and possible cAMP gradients at the nanometer scale. To assess intracellular cAMP diffusion under physiological conditions, we set out to directly measure cAMP dynamics in intact cells. We designed the cell-permeable, fluorogenic cAMP analog 8-(2-(5(6)-carboxyfluoresceindiacetate)-aminoethylthio)adenosine-3',5'-cyclic monophosphate (hereafter, 8-FDA-cAMP) which becomes fluorescent when hydrolyzed to the corresponding fluorescein compound 8-F-cAMP by intracellular esterases (**Figure 1A**). A detailed characterization of this compound is given in **Methods S1**, including optical properties, equivalence to cAMP in binding to and activation of PKA as well as resistance to degradation by PDEs.

The diffusion properties of this compound were then analyzed in intact cells by applying techniques that can report a wide range of diffusion speeds. Using a fluorescence fluctuation spectroscopy approach in combination with a confocal microscope, fast line-scan imaging of fluorescent molecules allows the precise extraction of diffusion coefficients ranging from below  $0.1 \mu\text{m}^2/\text{s}$  up to hundreds of  $\mu\text{m}^2/\text{s}$  (Ries et al., 2009, Hebert et al., 2005). (**Figures 1B and S1; STAR Methods**). Briefly, this approach yields the probability distribution function of an individual molecule occupying a given position in space and time (Spatiotemporal Image Correlation Spectroscopy (STICS) function): rapidly diffusing molecules can travel large distances in a short time, whereas bound or very slowly diffusing molecules persist at the same position for a long time. This method can capture combinations of different diffusion modes, or of diffusion

and binding, as schematically illustrated in **Figure 1C**. We calibrated the method using fluorescent compounds of known molecular weight, which yielded values in agreement with their theoretical diffusion coefficients in water (**Figure S1**).

To analyze cAMP dynamics in intact cells, we used this technology in HEK293 cells loaded with low concentrations (<100 nM) of 8-FDA-cAMP (**Figure S2**). These experiments revealed that, at low cAMP levels, virtually all cAMP displays a pattern reflecting a bound, i.e. largely immobile, state of cAMP (**Figures 1D and S2D**). This can be qualitatively appreciated by the long-time tail of the STICS function (**Figures 1C, 1D and S3**). This observation is very striking, since several studies have uniformly reported that cAMP diffuses very fast in cells (see **Table S1**). In stark contrast, our data suggest that at basal concentrations cAMP dynamics is severely constrained in cells.

Constrained cAMP diffusion in cells may be caused by cAMP binding to specific binding sites, resulting in ‘buffering’. To test whether such binding of 8-F-cAMP does indeed occur and would be overcome at higher cAMP concentrations by displacement from the binding sites, we stimulated HEK293 cells, after loading with 8-FDA-cAMP, with forskolin (fsk, 10  $\mu$ M) and IBMX (100  $\mu$ M) to maximally elevate intracellular cAMP levels. Analysis of cAMP dynamics under these stimulated conditions reveals a strikingly different spatiotemporal pattern: the long-time tail of the STICS function was largely lost, whereas a broader opening at shorter times was observed (**Figures 1E, S2E, and S3**). This fast component can also be appreciated by looking at diffusion coefficients extracted from the rapid time-scale of the Mean Square Displacement (MSD), and also by looking at the average transit time of the molecules over a distance of 1  $\mu$ m (**Figure 1F, S2E, and S2F**): this highlights fast cAMP diffusion (tens up to hundreds of  $\mu\text{m}^2/\text{s}$ ) in fsk/IBMX-

stimulated cells, similar to the diffusion speed of fluorescein. This is in stark contrast to cells under unstimulated conditions where cAMP appears virtually immobile (**Figure 1D, 1F**).

An alternative possibility to explain restricted cAMP diffusion might be geometrical diffusion constraints in cells (Richards et al., 2016). To rule out a contribution of such constraints, we collected STICS functions for 8-F-cAMP dynamics in cytosolic preparations under basal conditions (**Figure 2A**) and after saturating binding sites with unlabeled cAMP (**Figure 2B**). A set of reference molecules was used, spanning a range of molecular weights of approximately three orders of magnitude: fluorescein alone ( $\approx 0.3$  kDa), EGFP ( $\approx 25$  kDa) (**Figure 2C**) and Epac1-camps-PDE4A1 ( $\approx 120$  kDa) (**Figure 2D**). The diffusion coefficients obtained are displayed in **Figure 2E** as a function of their molecular weights. Based on the diffusion coefficient of the heaviest molecule ( $D = 27 \pm 2 \mu\text{m}^2/\text{s}$ ), we plotted the expected  $D$  values for the other molecules according to the Stokes-Einstein relationship, yielding the power law dependence  $D = MW^{-1/3}$  (dashed line). Interestingly, all molecules followed the expected free diffusion behavior with the notable exception of 8-F-cAMP. Here, the values are more than twice below the expected diffusion coefficient, indicating binding to heavier components of the cytosolic extracts, in the approximate average range of 10-50 kDa (shaded area in **Figure 2E**). Strikingly, 8-F-cAMP recovered its free diffusion value upon addition of 100  $\mu\text{M}$  unlabeled cAMP to block all presumed cAMP-binding sites in the cytosolic preparations (**Figures 2, S3**).

Such immobilization of cAMP requires high cAMP buffering capacity, and in fact, for the main cAMP effector PKA, such sites have been reported to occur in cell lysates in the low micromolar range (Walker-Gray et al., 2017). To quantify all cAMP binding sites, we estimated the buffering capacity of cytosolic preparations of HEK293 cells by titrating the concentration of 8-F-cAMP

and determining the bound vs. free ratio with steady-state anisotropy measurements (**STAR Methods, Figure S4**). Measurements done at two different dilutions of the cytosolic preparations gave a range of cytosolic cAMP binding sites of 6-15  $\mu\text{M}$  which is, as expected, larger than reported for PKA alone (Walker-Gray et al., 2017). The buffering capacity of entire cells (including particulate fractions such as membranes that are removed during cytosol preparations) is likely to be higher (Corbin et al., 1977). In our model, we make a conservative assumption of 20  $\mu\text{M}$  cAMP binding sites (**Methods S2**).

Together, these data indicate very significant binding of cAMP to intracellular binding sites. Under basal conditions and concentrations, cAMP is mostly bound, but if it gets displaced, it diffuses fast, compatible with diffusion rates observed in earlier studies.

#### **PDEs generate nanometer-sized cAMP gradients in intact cells**

We and others have shown that observed cAMP gradients in cells require the effective diffusion of cAMP to be restricted by orders of magnitude compared to what has been measured so far (Rich et al., 2000, Rich et al., 2001, Feinstein et al., 2012, Lohse et al., 2017, Xin et al., 2015). Our findings on cAMP dynamics (**Figures 1 and 2**) show that such restricted diffusion dynamics during the spatial spread of cAMP signals does indeed exist because of cAMP buffering. We reasoned that the resulting reduction of free cAMP might resolve these discrepancies, because they might facilitate the generation of local cAMP gradients by PDEs. This would provide the first direct experimental evidence of local cAMP gradient formation.

To visualize such gradients in intact cells and directly map their dimensions, we developed a set of genetically-encoded FRET-based *cAMP nanorulers*. Confocal images of all genetically-



encoded constructs in this study are compiled in **Figure S5M**. These sensors are composed of the FRET-based cAMP sensor Epac1-camps (Nikolaev et al., 2004) and a PDE, separated by single-alpha helical (SAH) domain linkers of defined nanometer length (**Figures 3A and 3B**). SAH domains are characterized by a modular sequence of ER/K amino acid repeats, resulting in a rod-like shape – which makes them ideally suited to spatially separate two protein moieties at a defined distance (Sivaramakrishnan and Spudich, 2011). Stimulation of endogenous  $\beta$ -adrenergic receptors ( $\beta$ -ARs) with isoproterenol in intact HEK293 cells led to an increase in cytosolic cAMP as measured by Epac1-camps (**Figure 3C**). Tethering a PDE4A1 directly to Epac1-camps completely blunted the isoproterenol-induced FRET response (**Figure 3E**). This must be specifically due to the tethered PDE4A1 activity, because, first, the specific PDE4-inhibitor roflumilast induced a large and robust FRET change of the Epac1-camps-PDE4A1 sensor (**Figure 3E**) and, second, stoichiometric overexpression of PDE4A1 with Epac1-camps without tethering them together still gave a robust (albeit dampened) FRET signal (**Figures 3D and 3G**). These data indicate that tethered PDE4A1 effectively depletes cAMP from the region surrounding the Epac1-camps sensor.

Strikingly, upon spatial separation of Epac1-camps and PDE4A1 by 10 nm (Epac1-camps-SAH10-PDE4A1), isoproterenol-stimulation induced a FRET response of almost the same amplitude as that seen with stoichiometric overexpression of both proteins individually (**Figures 3F and 3G**). As expected, inhibition of PDE4 activity in all constructs eliminated cAMP gradients (**Figure 3H**).

As controls to these experiments, we established that all constructs expressed equally well and that the described effects were similar at all expression levels (**Figure S5E**), and that fusion of neither PDE4A1 nor SAH10-PDE4A1 affects the affinity of Epac1-camps for cAMP (**Figure S5A**) nor

does fusion of SAH10 to PDE4A1 reduce catalytic activity (**Figure S5B-D**). We also showed that the effect of tethered PDE4A1 was lost in a catalytically inactive mutant (**Figure S5F and S5G**). The highly significant differences between tethered and either non-tethered or spacer-separated PDE4A1 (**Figure 3G**) strongly indicate that PDE4A1 creates a region of low cAMP concentration with a radius which is clearly smaller than 10 nm. We therefore define this as a *low cAMP nanodomain*.

#### **Low cAMP nanodomains are PDE-subtype-specific**

We reasoned that the size of such low cAMP nanodomains might be determined by the type of PDEs. While the PDE4 family studied above comprises high-affinity (low micromolar), but low turnover (1-5 cAMP/s) enzymes, the PDE2 family represents the fastest enzymes with regard to cAMP degradation (Bender and Beavo, 2006). Therefore, we fused a truncated version of PDE2A3, PDE2cat, comprising only its catalytic domain (aa 578-941), to Epac1-camps, thereby generating Epac1-camps-PDE2cat. In line with the findings obtained with PDE4, tethered PDE2cat activity blunted the cAMP-FRET response to isoproterenol relative to Epac1-camps alone (**Figures 4A vs 4C**). Only upon specific inhibition of PDE2 with BAY 60-7550 did Epac1-camps-PDE2cat detect an isoproterenol-mediated cAMP-increase (**Figure 4C**). Stoichiometric expression of both Epac1-camps and PDE2cat individually still led to a robust FRET signal upon isoproterenol stimulation (**Figure 4B**). These data confirm that also the tethered PDE2 activity generates a low cAMP nanodomain in its immediate vicinity (**Figure 4E**).

We then designed another cAMP nanoruler, Epac1-camps-SAH30-PDE2cat, which records cAMP levels at 30 nm distance to PDE2cat (**Figure 4D**). In contrast to the observations with Epac1-camps-SAH10-PDE4A1, we found a still significant effect on cAMP levels at 30 nm distance from

PDE2cat (Epac1-camps-SAH30-PDE2cat) (**Figures 4D and 4E**). As expected, inhibition of PDE2 activity in all constructs eliminated cAMP gradients (**Figure 4F**). To account for the higher catalytic activity of PDE2cat relative to PDE4A1, the PDE2cat experiments were performed at lower expression levels (**Figure S5H**). Again, we also showed that Epac1-camps-PDE2cat and Epac1-camps-SAH30-PDE2cat sensors were not compromised with regard to either cAMP affinity (**Figure S5I**) nor PDE catalytic activity (**Figure S5J-L**).

Combined, our data suggest that under basal conditions cells are able to buffer most of their cAMP. This, in turn, allows PDEs to generate low cAMP nanodomains. Only upon both, stimulation of ACs and inhibition of PDEs, is the level of cAMP raised sufficiently to overcome the capacity of the endogenous buffers and to progressively “flood” the small domains and ultimately entire cells.

We then aimed to assess whether such low cAMP nanodomains might also be demonstrated in cytosolic preparations and to quantify the concentration threshold at which they might become “flooded”, because PDEs are no longer able to establish significant cAMP gradients (**Figure 5**). Concentration-effect curves of cAMP-induced FRET changes of Epac1-camps are shown for the same conditions and constructs as used in cells for PDE4A1 (**Figure 5A**) and PDE2cat (**Figure 5B**), and the resultant shifts of the EC<sub>50</sub>-values are given in **Figure 5C**. These data show for Epac1-camps an apparent cAMP-affinity of 2.5 μM, which is shifted to 10-fold higher concentrations by tethered PDE4A1, while individual stoichiometric expression of Epac1-camps and PDE4A1 caused an only 2-fold affinity shift (**Figure 5A, C**). In line with the results obtained in intact cells, separating PDE4A1 from Epac1-camps by 10 nm reduced the shift to almost the same level as stoichiometric expression, i.e., essentially abolishing the specific nanodomains (**Figure 5A, C**). Analogous experiments performed with PDE2cat revealed a somewhat larger (15-fold) shift for

the directly tethered PDE, and here, as in cells, a 30 nm spacer only partially reduced the shift (**Figure 5B, C**). Inspection of the curves shows that the shifts exist also at higher cAMP concentrations, suggesting that the low cAMP nanodomains become fully “flooded” only at high concentrations of cAMP.

### **Low cAMP nanodomains control local PKA activity**

To investigate directly whether cAMP nanodomains translate into similarly targeted PKA signaling, we designed analogous targeted PKA activity reporters. Fusing PDE4A1 to the PKA FRET-sensor AKAR4 completely suppressed the detection of PKA activity in response to stimulation of HEK293 cells with isoproterenol, while AKAR4 alone gave a robust signal (**Figures 6A-D**). This indicates that the PDE “protects” the PKA in its immediate vicinity from the cAMP-stimulation.

To demonstrate that PDEs shape local PKA gradients, we used full-length PDE2A3. The long N-terminus of PDE2A3 should separate the catalytic center of the PDE from N-terminally fused sensors by several nanometers (Pandit et al., 2009). In fact, this construct allowed the respective sensors to again detect again isoproterenol-stimulated cAMP levels (**Figure 6E**) or PKA activity (**Figure 6F**). Interestingly, the constructs detected a comparable relative level of cAMP and of PKA activity (**Figure 6G**), strongly suggesting that the amount of cAMP at a given location in the cell dictates the degree of local PKA activity.

As controls for these experiments we showed that only inhibitors of the relevant tethered PDE lead to phosphorylation of the tethered PKA substrate, while inhibitors of other PDEs have no effect

(**Figure S6**). These data confirm the specificity of our results and illustrate that individual PDEs regulate cAMP signaling specifically in their immediate vicinity.

### **Model of cAMP signaling at the nanoscale**

To describe our findings in quantitative terms, we use a biophysical model for the formation of cAMP gradients by PDEs at the nanoscale (**Methods S2**). Based on our experimental observations (**Figures 1-3, S4**) this model analyzes the effects of binding sites on free cAMP concentrations in cells and on the spatial profile of cAMP gradients generated by PDE-mediated degradation.

The model confirms that cAMP gradients around PDEs are of nanometer size (see **Figure 7B, Methods S2**). **Figure 7B** illustrates the free cAMP concentration at a distance from the PDE4A1 (in red) superposed to the experimental free cAMP concentration ranges measured using our FRET sensors at the PDE, 10 nm away, and in the bulk of the cytosol. The concentration gradient follows the equation  $[cAMP] = [cAMP]_{bulk}(1 - R_0/r)$ , where  $[cAMP]$  denotes the concentration of free cAMP,  $[cAMP]_{bulk}$  the concentration of free bulk cAMP far from the PDE,  $r$  the distance from the PDE catalytic site, and  $R_0$  is a radius where  $[cAMP]$  would be equal to zero. This radius  $R_0$  relates not only to the geometrical size of the PDE but also to the flux of cAMP, i.e. the rate of degradation at the “sink” (see **Methods S2**).

Moreover, based on the cAMP concentration transients we obtain upon inhibition of PDE4A1 (see e.g. **Figure 3E**), we can infer a turnover number of ~320 molecules/s. To assess whether these PDE turnover rates are compatible with the model, we concomitantly addressed the question whether PDE4A1 exists in cells as mono- or oligomers. Molecular brightness analysis, a technique to extract molecular oligomerization (Annibale and Lohse, 2020), shows that Epac1-camps-

PDE4A1 is largely dimeric (in contrast to Epac1-camps alone; **Figure S7**). Therefore, our experiments and the biophysical model uniformly demonstrate that a single PDE4 has a turnover number of ~160 molecules cAMP/s in intact cells, which is sufficient to deplete a nanometer-sized region of cAMP and, thus, protects local cAMP effectors from being activated (**Figure 6**).

## DISCUSSION:

Despite a wealth of indirect evidence that cAMP compartments might exist in cells and should be under the control of PDEs, the molecular basis of how cAMP might be sequestered in cells has remained unknown for decades. Here, we provide the molecular mechanisms of such cAMP compartmentation at the nanoscale.

Our data introduce the novel concept that cellular cAMP is governed by catch-and-release or ‘buffered’ dynamics (**Figure 7A**). Under basal conditions, cAMP is mostly bound and effectively diffuses very slowly, if at all, and its free concentration is well below the levels of total cAMP, i.e. the levels measured by usual biochemical assays. When cAMP molecules are released from the binding sites, they diffuse fast – compatible with diffusion rates observed previously – but become re-captured quickly by the next cAMP binding proteins (**Figure 7A**, left panel). This is entirely compatible with earlier experiments, by us (e.g. (Nikolaev et al., 2004)) and others (**Table S1**), showing that rapid diffusion refers to the first time point at which a stimulus can be noticed in different areas of a cell; however, the corresponding signals continue to increase for long times afterwards, compatible with both continued production of cAMP and its slow effective diffusion. The experimental approach that we apply here has the advantage of using, for the first time, only trace amounts of fluorescent cAMP, not only allowing direct tracking of cAMP dynamics (as opposed to indirect tracking using FRET reporters), but also allowing measurements at or near basal cAMP levels, which permits us to clearly demonstrate buffered diffusion.

When cAMP levels are increased, for example by receptor stimulation, the binding sites become progressively saturated, free cAMP increases and diffusion occurs first from one binding site to the next and ultimately – once the binding sites become saturated – by free diffusion (**Figure 7A**,

right panel). Buffering of the initial cAMP wave ensures that free cAMP levels are kept in a range which then permits individual PDEs to create and “defend” a nanometer-sized space around them with an even lower concentration of cAMP, allowing effectors such as PKA to be “protected” from external cAMP-mediated stimuli within these nanometer-sized domains. Under these conditions, our data indicate that PDE catalytic rates are sufficient to metabolize the few free cAMP molecules that are present in these small volumes; when the ambient cAMP concentrations increase, the low cAMP domains become smaller. The downstream consequence of these nanometer-sized regions of low cAMP is that PKA (and presumably other cAMP effectors) remain insensitive to cAMP signals until cAMP is increased to levels that are sufficient to progressively fill these regions (see **Figure 7A**).

For our buffered diffusion model to hold, the requirement is that the buffering capacity of the cytoplasm is sufficient. In agreement with recent determinations (Walker-Gray et al., 2017) we directly determined the number of cytosolic cAMP binding sites to be in the range of 6-15  $\mu\text{M}$ . It has been shown that ~30-50% of the total cellular PKA are immobile and associated with the particulate fraction which we remove during our cytosol preparations (Corbin et al., 1977). Hence, the total amount of cAMP binding sites in cells is likely to be even higher than quantified here in cytosolic preparations. The discovery of the biomolecular condensates described in a companion manuscript strikingly illustrates additional “sponges” for cAMP (Zhang *et al.*, accompanying manuscript) which effectively increase the buffering capacity of the cell. Together, these sites are sufficient to very significantly buffer cellular cAMP levels - much alike the buffering of intracellular calcium, where also a large number of bindings sites reduce the free concentration and the effective diffusion rate of calcium ions (Wagner and Keizer, 1994).



Calculation of a concentration gradient around a single PDE4A1, based on the Smoluchowski model (Smoluchowski, 1916, Rice, 1985) (**Methods S2**), shows that a nanometer-sized region of significantly lowered cAMP does indeed occur (**Figure 7B**). Given the largely dimeric PDE4A1 structure, our data therefore indicate that the measured cAMP concentration values in the bulk and at the tethered FRET-sensor are in agreement with an individual PDE4A1 turnover rate of about 160 molecules/s. Although this is higher than values reported for the purified enzyme (Bender and Beavo, 2006), these latter values may well be reduced due to damage during purification, while ours are some of the first data providing individual PDE4 turnover rates in intact cells, and as such not conflict with previous literature values. In fact, in intact cells, very high PDE activities have already been reported (Nikolaev et al., 2005). The excellent agreement of the data of the cAMP measurements in intact cells and in cytosolic preparations (see **Methods S2**) further supports this conclusion.

The agreement of the size of low cAMP nanodomains with that of the PKA activity measured with the AKAR4 sensor suggests that nanometer-sized PDE domains indeed modulate downstream target activation and may represent functional modules of cAMP signaling. The demonstration of such functional cAMP and PKA nanodomains is further in line with recent observations by super-resolution microscopy of PKA signaling hot-spots with a diameter of 100-200 nm (Mo et al., 2017). To constrain PKA activity to such small domains requires that its catalytic subunit is either rapidly recaptured by the regulatory subunits after activation (Mo et al., 2017, Walker-Gray et al., 2017), or that PKA can function as an intact holoenzyme (Smith et al., 2017).

Our data with PDE2 demonstrate that longer-range effects of PDEs may also be possible, both for cAMP and PKA signals. The mechanisms of these longer range effects needs to be explored further, but we would like to note the possibility of a larger effective radius (possibly due to the

fact that in these experiments we used only isolated catalytic domains of PDE2, unlikely to remain immobile in intact cells because of lack of targeting domains) or of more complex arrangements. However, the excellent agreement of the data from intact cells and cytosolic preparations suggests that these observations are indeed a property of our PDE2 constructs.

Our demonstration of sharp concentration gradients along with a direct translation into graded PKA activity explains how cAMP can act very locally, and thus trigger responses spatially limited at the nanometer scale. The very small size of cAMP domains strongly suggests that compartmentalized cAMP signaling is controlled in a stochastic manner by individual molecules of cAMP. This spatially tight control provides the basis for the physiologically important specificity of cAMP signaling. Disruption of local cAMP signaling has been suggested to be associated with a variety of diseases (Gold et al., 2013) such as heart failure (Nikolaev et al., 2010) and cancer (Zhang et al., companion manuscript). The elucidation of the molecular basis of cAMP compartmentation now permits to link disruption of cAMP compartmentation to disease and, thus, to explore novel therapeutic strategies that are based on a cell's ability to orchestrate cAMP signaling in nanometer-sized domains.

**ACKNOWLEDGMENTS:**

We thank Dr. Frank Schwede, Biolog GmbH, Germany, for discussion on the design of 8-FDA-cAMP, and all members of the Lohse lab for critical discussions. We are grateful to Dr. Carmine Di Rienzo for discussion and constructive input on data analysis. This work was supported by the European Research Council (Grant TOPAS, to M.J.L.), the German Research Foundation (Deutsche Forschungsgemeinschaft; SFB688 to M.J.L.; SFB1423 to A.B., P.A. and M.J.L.).

**AUTHOR CONTRIBUTIONS:**

A.B., P.A., and M.J.L. conceived of the project and designed the methodology. A.B., P.A., C.K., A.H., and S.E.A. conducted investigations and formal analyses. U.Z. provided guidance in cloning strategies. I.M. contributed to the design of the methodology. S.S. provided guidance in preparation and use of SAH linkers. M.F. developed the biophysical model. A.B., P.A., and C.K. prepared data visualization. A.B., P.A. and M.J.L. wrote the manuscript with edits from C.K. and M.F. M.J.L. initiated the project. A.B., P.A., M.F. and M.J.L. supervised research. A.B. and M.J.L. administered the project.

**DECLARATION OF INTERESTS:**

The authors declare no competing interests.

## FIGURES AND LEGENDS:

**Figure 1. cAMP dynamics are highly restricted in intact cells.** (A) Molecular structure of fluorogenic 8-FDA-cAMP. Arrows highlight sites where intracellular esterases cleave both ester bonds. (B) Linescan approach used in our experiments. The focused laser beam (blue ellipsoids) is repeatedly scanned along the cell cytosol, giving rise to a kymograph containing the 8-FDA-cAMP fluorescence fluctuations (see **STAR Methods**) (C) Two simulated STICS functions are schematically illustrated, referring to fast ( $100 \mu\text{m}^2/\text{s}$ ) diffusion rates combined with binding (left) and fast diffusion rates alone (right). x-axis refers to the spatial, y-axis to the temporal dimension. (D) Average STICS function (11 different cells, three independent experiments) measured in the cytoplasm of intact HEK293 cells loaded for 30 min with 100 nM 8-FDA-cAMP under basal conditions. (E) Average STICS function (9 different cells, three independent experiments) measured in the cytoplasm of intact HEK293 cells loaded for 30 min with 100 nM 8-FDA-cAMP and stimulated for 5 min with fsk (10  $\mu\text{M}$ )/IBMX (100  $\mu\text{M}$ ). (F) Measured diffusion coefficient in HEK293 cells extracted from the slope of the MSD in the range of 0-0.5 ms for FDA, 8-FDA-cAMP (from panel D) and 8-FDA-cAMP stimulated with fsk + IBMX (from panel E). Error bars are standard deviations.

**Figure 2. cAMP dynamics are buffered via cAMP binding sites.** Average STICS function measured in a cytosol preparation of (A) HEK293 cells loaded for 30 min with 100 nM 8-FDA-cAMP (n=8). (B) as in (A) after the addition of unlabeled cAMP (100  $\mu\text{M}$ ) (n=6). (C) HEK293 cells expressing EGFP (n=6) and (D) HEK293 cells expressing the fusion protein Epac1-camps-PDE4A1 (n=4). (E) Relationship between molecular weight and diffusion coefficients. Orange crosses represent the diffusion coefficients extracted from the fit of the average STICS function

(Eq. 1, STAR Methods) derived from panels (A-D) and FDA alone. The diffusion coefficients are plotted against the molecular weight of each compound. Red dots represent the theoretical diffusion coefficients based on the Stokes-Einstein relation  $D = \frac{kT}{6\pi\eta R}$ . The power law dependence on the molecular weight (exponent = -0.3) is superimposed to the data as a blue dotted line.

**Figure 3. Genetically-encoded nanorulers map cAMP gradients around single PDE molecules in intact cells.** (A,B) Design of FRET-based nanorulers to identify low cAMP nanodomains in intact cells. Tethering the FRET-based cAMP sensor Epac1-camps to a PDE allows measuring cAMP concentrations in the direct vicinity of a single PDE molecule (A). Incorporation of nanometer linkers based on single alpha helical domains between Epac1-camps and a PDE allows measuring the cAMP gradient at defined distances away from the PDE (B). (C) Isoproterenol (Iso, 10  $\mu$ M) stimulation leads to an increase in cAMP levels which are detected by Epac1-camps (note upward-reflected trace). (D) When Epac1-camps and PDE4A1 are expressed at equimolar levels but not tethered, a rise in cAMP levels is still detected upon Iso stimulation. (E) However, when tethering PDE4A1 to Epac1-camps (which measures cAMP levels in direct vicinity of PDE4A1), no rise in cAMP is detected upon Iso stimulation. (F) Separating Epac1-camps and PDE4A1 with a 10 nm linker leads to a similar response than observed in the equimolar expression in (D). (C-F) Average traces of corrected and normalized FRET ratios in HEK293 cells transfected with Epac1-camps (C), Epac1-camps-IRES2-PDE4A1 (i.e. individual but roughly equimolar expression of sensor and PDE) (D), Epac1-camps-PDE4A1 (= tethered) (E), and Epac1-camps-SAH10nm-PDE4A1 (=10 nm distance) (F), treated consecutively with isoproterenol (Iso, 10  $\mu$ M), the PDE4-inhibitor roflumilast (300 nM), and fsk (10  $\mu$ M)/IBMX (100  $\mu$ M). Traces are representative for 8, 13, 19, and 14 independent experiments, respectively. The solid lines indicate the mean, shaded areas the s.e.m. FRET traces are normalized to baseline (set to 0%) and maximal

stimulation upon fsk/IBMX treatment (set to 100%). The inset in (C) shows the normalized, isoproterenol-induced FRET ratios from all cells expressing Epac1-camps (n=34). (G,H) Normalized, isoproterenol-induced (G) or roflumilast-induced (H) FRET ratios pooled from all cells measured as in (D-F). n=63 (Epac1-camps-IRES2-PDE4A1), 56 (Epac1-camps-PDE4A1), and 51 (Epac1-camps-SAH10nm-PDE4A1) cells. The columns represent means, the vertical bars s.e.m. \*\*\*\*P<0.0001, one-way analysis of variance (ANOVA, Tukey's post-test), n.s. not significant.

**Figure 4. Low cAMP nanodomains are PDE-subtype-specific.** (A) Iso stimulation leads to an increase in cAMP levels which are detected by Epac1-camps (note upward-reflected trace). (B) When Epac1-camps and PDE2cat are expressed at equimolar levels but not tethered, a rise in cAMP levels is still detected upon Iso stimulation. (C) However, when tethering PDE2cat to Epac1-camps, no rise in cAMP levels is detected upon Iso stimulation. (D) Separating Epac1-camps and PDE with a 30 nm linker leads to almost no Iso-induced FRET response similar to what is observed in (C). (A-D) Average traces of corrected and normalized FRET ratios in HEK293 cells transfected with Epac1-camps (A), Epac1-camps-IRES2-PDE2cat, leading to individual but roughly equimolar expression of the two proteins (B), Epac1-camps-PDE2cat (tethered) (C), and Epac1-camps-SAH30nm-PDE2cat (D), treated consecutively with isoproterenol (Iso, 10  $\mu$ M), the PDE2-inhibitor BAY 60-7550 (100 nM), and fsk (10  $\mu$ M)/IBMX (100  $\mu$ M). Traces are representative for 3, 10, 11, and 14 independent experiments, respectively. The inset in (A) shows the normalized, isoproterenol-induced FRET ratios from all cells expressing Epac1-camps (n=12). The solid lines indicate the mean, shaded areas s.e.m. FRET traces are normalized to baseline (set to 0%) and maximal stimulation upon fsk/IBMX treatment (set to 100%). (E,F) Normalized, isoproterenol-induced (E) and BAY 60-7550-induced (F) FRET ratios pooled from all cells

measured as in (B-D). n=28 (Epac1-camps-IRES2-PDE2cat), 30 (Epac1-camps-PDE2cat), and 25 (Epac1-camps-SAH30nm-PDE2cat) cells. The columns represent means, the vertical bars s.e.m. \*\*\*\*P<0.0001, \*\*\*P<0.001 one-way analysis of variance (ANOVA, Tukey's post-test), n.s. not significant.

**Figure 5. Low cAMP nanodomains stay intact in cytosolic cell preparations and become 'flooded' at micromolar cAMP.** (A,B) Shown are concentration-effect curves of cAMP-induced changes in FRET ratio normalized to buffer (set to 0%) and 1 mM cAMP (set to 100%). (A) Tethering PDE4A1 (blue curve) to Epac1-camps (black curve) leads to a pronounced right-shift of the concentration-effect curve, much more than stoichiometric overexpression of Epac1-camps and PDE4A1 (+PDE4A1, green curve). The difference in the EC<sub>50</sub>-values between the green (global PDE activity) and blue curves (local PDE activity) is a biochemical equivalent to the cAMP nanodomain. Separating Epac1-camps and PDE4A1 by 10 nm (Epac1-camps-SAH10nm-PDE4A1) does not generate a low cAMP nanodomain (turquoise curve). Note that the turquoise curve (cAMP at 10 nm distance from the PDE) and the green curve (global PDE activity) are superimposable. (B) Tethering PDE2cat (red curve) to Epac1-camps (black curve) leads to a pronounced right-shift of the concentration-effect curve, significantly more than individual stoichiometric expression of Epac1-camps and PDE2cat (yellow curve). Separating Epac1-camps and PDE2cat by 30 nm (Epac1-camps-SAH30nm-PDE2cat, orange curve) only partially restores the cAMP gradient. Note that the orange line (cAMP at 30 nm distance from the PDE) is in between the dashed yellow (global PDE activity) and red lines (local PDE activity). Data in (A,B) are means ± s.e.m. of at least three independent experiments. (C) Apparent cAMP EC<sub>50</sub> values derived from the data in (A, B). The mean EC<sub>50</sub> of Epac1-camps is shown as a solid black line. Bars show the mean cAMP EC<sub>50</sub> values for stoichiometric expression of Epac1-camps plus

PDE4A1/PDE2cat expressed separately (+), with tethered PDE4A1 or PDE2cat, respectively (tethered), and at a distance of 10 and 30 nm from the PDEs (10 nm and 30 nm). Error bars show the 95% confidence intervals of the mean.

**Figure 6. Low cAMP nanodomains dictate local PKA activity.** (A) Design of nanodomain-targeted PKA activity reporters. (B-D) The PDE4A1/cAMP nanodomain completely blunts local PKA-dependent phosphorylation. Average traces of corrected and normalized FRET ratios in HEK293 cells transfected with AKAR4 (B) and AKAR4-PDE4A1 (C), treated consecutively with isoproterenol (Iso, 10  $\mu$ M), roflumilast (300 nM, in (C) only), and fsk (10  $\mu$ M)/IBMX (100  $\mu$ M). Traces are representative for 3 and 5 independent experiments, respectively. The solid lines indicate the mean, shaded areas the s.e.m. FRET-traces are normalized to baseline (set to 0%) and maximal stimulation upon fsk/IBMX treatment (set 100%). (D) Normalized, isoproterenol-induced FRET ratios pooled from all cells measured as in (B,C). n=20 (AKAR4) and 22 (AKAR4-PDE4A1) cells. The horizontal bars represent means, the vertical bars s.e.m. \*\*\*\*P<0.0001, unpaired t-test. (E-G) Local cAMP pools spatially overlap with local PKA phosphorylation. (E, F) Average time courses of corrected and normalized FRET ratios in HEK293 cells transfected with Epac1-camps-PDE2A3 (E) and AKAR4-PDE2A3 (F), treated consecutively with isoproterenol (Iso, 10  $\mu$ M), BAY 60-7550 (100 nM), and fsk (10  $\mu$ M)/IBMX (100  $\mu$ M). Time courses are representative of 8 and 7 independent experiments, respectively. The solid lines indicate the mean, shaded areas s.e.m. FRET traces are normalized to baseline (set to 0%) and maximal stimulation upon forskolin/IBMX treatment (set to 100%). (G) Normalized, isoproterenol-induced FRET ratios pooled from all cells measured as in (E,F). n=32 (Epac1-camps-PDE2A3) and 35 (AKAR4-PDE2A3) cells. The horizontal bars represent means, the vertical bars s.e.m.



**Figure 7. Model of cAMP signaling at the nanoscale.** (A) Schematic illustration of buffered diffusion of cAMP and formation of low cAMP nanodomains under basal (left) and stimulated conditions (right). The presence of a large concentration of cAMP binding sites (illustrated as honeycombs) (**Figure S4**) lowers the concentration of free cAMP (red dots). The low concentration of free cAMP enables phosphodiesterases to establish nanometer-sized domains where the local cAMP concentration is decreased to a range below the activation threshold of local cAMP effectors (lower panels). Upon stimulation (right panel), cAMP binding sites become progressively saturated and, as a consequence, the width and depth of these nanodomains is decreased, eventually leading to “flooding” and activation of local cAMP effectors. (B) The spatial cAMP concentration profile (red line) around a PDE4A1 molecule as inferred from experiments (**Figure 3**) and quantitative considerations (**Methods S2**). The red line shows the free cAMP concentration profile generated by a PDE4A1 dimer with a turnover rate of ~160 molecules/s/PDE4A1. The gray shaded area illustrates the range of possible profiles from experimental values (**Methods S2**). The open blue circles represent the measured mean values of free cAMP concentration at the PDE4A1 (data from **Figure 3E**), at 10 nm distance of the PDE (data from **Figure 3F**), and in bulk cytosol (data from **Figure 3D**). Error bars represent 95% confidence intervals. The black line indicates the cAMP concentration profile around a perfect absorber (**Methods S2, Eq. 3**). The inset shows the same data with a linear x-axis.

## SUPPLEMENTAL FIGURE TITLES AND LEGENDS

**Figure S1. Related to Figures 1 and 2. Concept for measuring diffusion coefficient of a fluorescent species based on sequential rapid linescans and STICS measurement of the diffusion of a set of reference molecules of known molecular weight in water: experiments and theory.**

(A) Simulated STICS function derived for a species undergoing free diffusion in 3D at a rate of  $50 \mu\text{m}^2/\text{s}$ , (B)  $1 \mu\text{m}^2/\text{s}$  and (C)  $0.1 \mu\text{m}^2/\text{s}$ . (D) Measured (Gaussian) profiles of the STICS functions in (A) and (C) at four different times highlighted by the dashed lines, namely 1 ms (red), 10 ms (yellow), 100 ms (green) and 1 s (blue). (E) From the broadening of the Gaussians measured at increasing time lags, it is possible to reconstruct a MSD (**eq. 1**). (F) This approach is graphically summarized using a color code referring to the curves in (D). (G) Vertical cross sections of the STICS functions in (A), illustrating the shift to the right of the distribution of arrival times as the diffusion coefficient is reduced from  $50 \mu\text{m}^2/\text{s}$  to  $0.1 \mu\text{m}^2/\text{s}$ . (H) Average STICS functions (3 independent experiments) of 100 nM fluorescein, 100 nM 20kDa fluorescein-dextran, 100 nM 70kDa fluorescein-dextran and of 100 nM 250kDa fluorescein-dextran measured in water. The pH was set to pH=9 using NaOH and the measurements performed at room temperature ( $T=25^\circ\text{C}$ ). (I) Least-squares one-diffusion component fit (**eq. 1**) of the STICS functions displayed in (H). (J) Mean squared displacement (MSD) from the STICS functions in (H) (with exception of fluorescein, which is too fast for this line by line fitting and **eq. 1** was used). (K) Distribution of arrival times over a distance of  $1 \mu\text{m}$  for FDA, 20 kDa, 70 kDa, 250 kDa fluorescein-dextran molecules respectively.

(L) Red crosses display diffusion coefficients extracted from the data displayed in (H) as a function of the molecular weight. Blue circles represent the predicted diffusion coefficients for these molecules as derived from the literature (Arrio-Dupont et al., 1996).

**Figure S2. Related to Figure 1. Cellular uptake kinetics and distribution of FDA and 8-FDA-cAMP and multi-scale cAMP dynamics in intact cells.** (A) Fluorescence intensity time course recorded in a Neo2 plate reader (see **STAR Methods**) from a population of HEK293 cells incubated with 100 nM FDA (red), 100 nM 8-FDA-cAMP (blue), or HBSS (black), respectively. (B) Confocal and corresponding DIC images of HEK293 cells loaded with 100 nM of 8-FDA-cAMP (B) or 100 nM FDA (C) after 30 minutes of incubation and washout in HBSS. Scale bars are 10  $\mu\text{M}$ . (D) The broadening of the STICS function in **Figure 1D** (basal) as a function of time is recorded by displaying its horizontal cross sections at selected time points, as indicated by the color scale. (E) Same as in (D), for the STICS functions in **Figure 1E** (stimulated, i.e. fsk (10  $\mu\text{M}$ )/IBMX (100  $\mu\text{M}$ )). (F) Distribution of average molecular arrival times extracted from the vertical profiles of **Figures 1D** and **1E** at a distance of 1  $\mu\text{m}$ . (G) MSD for the basal and fsk/IBMX stimulated case for the 0-2 ms range. (H) Simulated STICS function for the combined diffusion of a fast (150  $\mu\text{m}^2/\text{s}$ ) and a slow (0.1  $\mu\text{m}^2/\text{s}$ ) components and (I) resulting MSD with linear fits to the two components: fast (blue), slow (red).

**Figure S3. Related to Figures 1 and 2. STICS functions of 8-FDA-cAMP in intact HEK293 cells and cytosolic preparations.** (A) Shown are nine representative STICS functions for 8-F-cAMP dynamics in HEK293 cells under basal conditions. (B) Shown are nine representative STICS functions for 8-F-cAMP dynamics in HEK293 cells after 5 minutes stimulation with fsk (10  $\mu\text{M}$ )/IBMX (100  $\mu\text{M}$ ). (C) Representative STICS functions for 8-F-cAMP dynamics in HEK293 cell cytosolic preparations in basal conditions and (D) after addition of 100  $\mu\text{M}$  unlabeled cAMP. (E) 2D least squares fit to the STICS functions reported in **Figures 2A-2D** using **eq. 1**. The temporal axes of fits are reported in linear scale, to facilitate comparison.

**Figure S4. Related to Figures 2 and 7. Quantification of the buffering capacity of cytosolic preparations using anisotropy.** Cytosolic preparations were prepared (**STAR Methods**) and diluted in binding buffer (20 mM MOPS, 150 mM NaCl, 0.005 % CHAPS, 0.5 mM IBMX, pH 7) (for details on dilutions see **STAR Methods**). Increasing amounts of 8-F-cAMP lead to a decrease in anisotropy values, both in the 60x and 1500x diluted cytosolic preparations. The reduction in anisotropy is ascribed to the increasing ratio of free 8-F-cAMP vs bound 8-F-cAMP (at low concentrations of 8-F-cAMP, essentially all 8-F-cAMP is bound (measured by high anisotropy values) because the concentration of the dye is well below the concentration of the cAMP binding sites (i.e. the buffering capacity) in the cytosolic preparation). At increasing concentrations of 8-F-cAMP the buffering capacity of the cytosolic preparation is exceeded, and the anisotropy values decrease towards those of free 8-F-cAMP. Data are normalized to the maximal anisotropy value in order to account for the different anisotropy values observed at the two different dilutions of cytosolic preparations. Fluorescein alone does not display any binding. Solid lines connecting the mean values are meant as a guide for the eye. Data are mean  $\pm$  s.e.m. from three independent experiments.

**Figure S5. Related to Figures 3 and 4. Affinities, catalytic activities and expression levels of FRET biosensors.** (A-D) *PDE4A1* sensors are neither compromised in cAMP affinity nor catalytic PDE activity. (A) Tethering PDE4A1 (blue) or SAH10-PDE4A1 (turquoise) to Epac1-camps (black) does not change the affinity of the sensor for cAMP. Shown are concentration effect curves of the normalized emission ratios (480/525 nm) obtained from cytosolic fractions of HEK293 cells expressing the indicated constructs (pre-incubated with 100  $\mu$ M IBMX) in the

presence of the indicated cAMP concentrations. Data are means  $\pm$  s.e.m. of at least 3 independent experiments. (B,C) The catalytic activity of PDE4A1 is not altered when tethered to Epac1-camps (B) or Epac1-camps-SAH10 (C). Data show one representative (out of 6-9) emission ratios (CFP/FRET) measured over time in cytosolic fractions of transfected HEK293 cells. Addition of 100  $\mu$ M cAMP (black arrow) leads to an increase in the emission ratio which is transient due to PDE4A1 activity. (D) The 'dwell' times ( $\Delta t$ ; mean  $\pm$  s.e.m.) are a surrogate parameter for PDE activity and are not significantly different in the two constructs, according to an unpaired t-test. (E) *Dependence of FRET-responses to isoproterenol on PDE4A1 expression levels.* Shown are normalized FRET ratios (CFP/FRET) upon isoproterenol (10  $\mu$ M) stimulation of HEK293 cells transiently transfected with the indicated constructs, normalized to the maximum response elicited upon fsk (10 $\mu$ M)/IBMX (100  $\mu$ M) stimulation. Data points show isoproterenol responses from all cells measured in **Figure 3**. Only cells expressing the respective sensor at expression levels resulting in YFP emission values of 1500-4000 were used for the analysis. In this range, sensor expression has only a slight negative effect upon isoproterenol responses. Green: Epac1-camps + PDE4A1, blue: Epac1-camps-PDE4A1, turquoise: Epac1-camps-SAH10-PDE4A1. (F, G) *A fusion protein of Epac1-camps and a catalytically-dead PDE4A1 (D352A) senses cAMP.* (F) Epac1-camps-PDE4A1 (D352A) senses cAMP increases upon Iso stimulation. Shown is an average trace from one representative coverslip (3 cells) of corrected and normalized FRET ratios in HEK293 cells transiently transfected with the indicated construct. The solid line indicates the mean, shaded areas the s.e.m. Cells were treated consecutively with isoproterenol (Iso, 10  $\mu$ M), the PDE4-inhibitor roflumilast (300 nM) and forskolin (fsk, 10  $\mu$ M)/IBMX (100  $\mu$ M). An increase in FRET, which is comparable to the experimental data of Epac1-camps (c.f. **Figure 3C**), was obtained directly after Iso addition. (G) Iso-induced FRET responses from experiments in (F) were

normalized to FRET responses induced by fsk/IBMX (set as 100 %). Data are means  $\pm$  SD from 11 cells. (H) *Dependence of FRET-responses on PDE2cat expression levels.* Shown are normalized FRET ratios (CFP/FRET) upon isoproterenol stimulation of HEK293 cells transiently transfected with the indicated constructs, normalized to the maximum response elicited upon fsk (10  $\mu$ M)/IBMX (100  $\mu$ M) stimulation. Data points show isoproterenol responses from all cells measured in **Figure 4**. Only cells expressing the respective sensor at expression levels resulting in YFP emission values of 25-800 were used for the analysis. In this range, sensor expression has only a slight negative influence upon isoproterenol responses, while FRET changes could still be robustly detected. Yellow: Epac1-camps + PDE2cat, red: Epac1-camps-PDE2cat, orange: Epac1-camps-SAH30-PDE2cat. (I-L) *PDE2cat sensors are neither compromised in cAMP affinity nor catalytic PDE activity.* (I) Tethering PDE2cat (red) or SAH30-PDE2cat (orange) to Epac1-camps (black) does not change the affinity of the sensor for cAMP. Shown are concentration-effect curves of the normalized emission FRET ratios (480/525 nm) obtained from cytosolic fractions of HEK293 cells expressing the indicated constructs (pre-incubated with the PDE2-inhibitor EHNA (100  $\mu$ M) in the presence of indicated cAMP concentrations. Data are means  $\pm$  s.e.m. of at least 3 independent experiments. (J,K) The catalytic activity of PDE2cat is not altered when tethered to Epac1-camps (J) or Epac1-camps-SAH30 (K). Data show one representative (out of 7) emission ratios (CFP/FRET) measured over time in cytosolic fractions of transfected HEK293 cells. Addition of 100  $\mu$ M cAMP (black arrow) leads to an increase in the emission ratio which is transient due to PDE2cat activity. (L) The 'dwell' times ( $\Delta t$ ; mean  $\pm$  s.e.m.) are a surrogate parameter for PDE activity and not significantly different in both constructs, according to an unpaired t-test. (M) *Confocal images of all FRET-based biosensors used in this study.* Indicated FRET-based biosensors were transiently expressed in HEK293 cells and fluorescence from each

construct (excited using direct EYFP excitation at 514 nm) is displayed next to the Differential Interference Contrast image (DIC). Scale bar is 10  $\mu\text{m}$ . For single-cell FRET experiments, regions of interest (ROIs) were selected taking care to analyze only regions of homogeneous expression (see example in panel M).

**Figure S6. Related to Figure 6. PDE4A1 and PDE2A3 abolish PKA activity only in their immediate vicinity.** (A-C) Inhibition of local PDE4A1 activity with the PDE4-inhibitor roflumilast leads to strong local PKA activity in the PDE nanodomain (A, also cf **Figure 6**) whereas treatment with the PDE2-inhibitor BAY 60-7550 has no effect (B, C). (D-F) Inhibition of local PDE2A3 activity with the PDE2-inhibitor BAY 60-7550 leads to strong local PKA activity in the PDE nanodomain (D, also cf **Figure 6**) whereas treatment with the PDE4-inhibitor roflumilast has no effect (E, F). Shown are representative traces of normalized FRET ratios measured in HEK293 cells transiently transfected with AKAR4-PDE4A1 (A-C) and AKAR4-PDE2A3 (D-F). Cells were treated consecutively with indicated compounds (isoproterenol (Iso, 10  $\mu\text{M}$ ), PDE-inhibitors (PDE4: roflumilast (300 nM), PDE2: BAY 60-7550 (100 nM)), and fsk (10  $\mu\text{M}$ )/IBMX (100  $\mu\text{M}$ )). Traces show one representative coverslip with (A) 6 cells, (B) 7 cells, (C) 5 cells, (D) 4 cells, (E) 3 cells and (F) 4 cells out of three independent experiments. Solid lines indicate the mean, shaded areas the s.e.m.

**Figure S7. Related to Figure 7. Characterization of the oligomerization state of PDE4A1.** Shown are molecular brightness data of HEK293 cells transiently expressing Epac1-camps-IRES2-PDE4A1 (stoichiometric expression of Epac1-camps and PDE4A1, red circles) or Epac1-camps-PDE4A1 (tethered PDE4A1, blue rectangles). The average molecular brightness of Epac1-

camps (measured by direct excitation of EYFP at 514 nm), which defines the monomeric state is 2324 photon counts/molecule/s, whereas the average molecular brightness of Epac1-camps-PDE4A1 is 5009 photons/molecule/s, indicating on average a dimer or higher order oligomers. Red circles and blue rectangles correspond to one measurement of one intact cell. Three separate transfections were investigated for each construct. Solid black lines represent the mean, error bars s.e.m.

**Table S1. Related to Figures 1 and 2. cAMP diffusion coefficients (in  $\mu\text{m}^2/\text{s}$ ) in living cells reported in the literature**

**Table S2. Related to STAR Methods. Oligonucleotides used for biosensor construction.**



## **STAR METHODS**

### **RESOURCE AVAILABILITY**

#### *Lead Contact*

Further information and requests for resources and reagents should be directed to and will be fulfilled by the Lead contact, Martin J. Lohse (m.lohse@mdc-berlin.de).

#### *Materials Availability*

Plasmids generated in this study are available from the authors upon request.

#### *Data and Code Availability*

The published article includes all datasets generated or analyzed during this study. For some data analysis we used a custom code/algorithm implemented in IGOR Pro, as previously published (Di Rienzo and Annibale, 2016), (Serfling et al., 2019), (Bathe-Peters et al., 2020), which is available from the authors upon request.

### **EXPERIMENTAL MODEL AND SUBJECT DETAILS**

HEK-tsA201 cells (ECACC 96121229 from Sigma-Aldrich Chemie GmbH), indicated as HEK293 throughout the manuscript, were cultured in Dulbecco's modified Eagle Medium (DMEM) with 4.5 g/L glucose (PAN biotech, Aidenbach, Germany), 10 % fetal bovine serum (Biochrom GmbH, Berlin, Germany), 100 U/ml penicillin, 100 µg/mL streptomycin (Pen/Strep, Gibco Life technologies, Carlsbad, CA, USA) and 2 mM-glutamine (PAN biotech, Aidenbach, Germany) at 37°C and 5% CO<sub>2</sub>. Cells were passaged in T75 flasks (SARSTEDT, Nümbrecht, Germany) every 2-4 days when reaching a confluency of 80-90%. Cells were routinely tested for

mycoplasma contamination using MycoAlert™ Mycoplasma Detection Kit from Lonza (Basel, Switzerland). Cell lines were not contaminated with mycoplasma.

For single-cell FRET measurements HEK293 cells were plated on 24 mm glass coverslips (Fisher Scientific GmbH, Waltham, MA, USA) in 6-well-dishes (SARSTEDT, Nümbrecht, Germany) at a density of approximately  $2 \times 10^5$  cells/mL. Transfection of plasmids (600 ng for Epac1-camps-based constructs, 300 ng for AKAR4-based constructs) was carried out 6 h after seeding using the Effectene Transfection Reagent (Qiagen GmbH, Venlo, Netherlands) according to the manufacturer's instructions. After 18-24 h, cells were used for imaging.

For FRET measurements in cytosolic preparations, HEK293 cells were plated on 100 mm dishes (SARSTEDT, Nümbrecht, Germany) to give a density of approximately 50-60%. 8 h later cells were transfected with a total amount of 20 µg cDNA (10 µg cDNA encoding the gene of interest and 10 µg pcDNA3) using calcium phosphate precipitation. 48 h after transfection, cells were used for experiments.

## **METHOD DETAILS**

### ***Synthesis and characterization of 8-F-cAMP***

The designed fluorogenic cAMP analogue *8-(2-(5(6)-carboxyfluoresceindiacetate)-aminoethylthio)adenosine-3',5'-cyclic monophosphate* (abbreviation: **8-FDA-cAMP**) was custom-synthesized by Biolog Life Science Institute, Bremen, Germany (details in **Methods S1**). The identity and purity of 8-FDA-cAMP were assessed with mass spectrometry and HPLC, respectively, by Biolog Life Science Institute, Bremen, Germany (details in **Methods S1**).

8-F-cAMP (the de-esterified fluorescent analogue of the membrane-permeable prodrug 8-FDA-cAMP) was used for the photophysical and biochemical characterization. To provide the photophysical characteristics of 8-F-cAMP, we recorded the absorption, excitation, and emission

spectra of 8-F-cAMP (details in **Methods S1**). To determine the binding affinity of 8-F-cAMP to its binding protein PKA regulatory subunit I alpha (PKA-RI $\alpha$ ), we performed steady state anisotropy measurements (details in **Methods S1**). To show that 8-F-cAMP activates downstream signaling, we used the PKA Colorimetric Activity Kit (ThermoFisher Scientific, Waltham, MA, USA) which reports on the activation of endogenous PKA in HEK293 cell lysates (details in **Methods S1**). To determine the stability of 8-F-cAMP towards hydrolysis by PDEs, we conducted PDE activity assays using a purified PDE from bovine brain and a colorimetric PDE assay (PDELight<sup>TM</sup>, Lonza) (details in **Methods S1**).

#### *cDNAs and biosensor construction*

The cDNA encoding PDE2A (NM\_002599) was purchased from OriGene, Rockville, MD, USA. The AKAR4 plasmid (Depry et al., 2011) was a kind gift of Dr. Jin Zhang (UC San Diego, USA) and a plasmid encoding the IRES2 sequence was kindly provided by Dr. Gary Lewin (MDC Berlin, Germany).

To generate Epac1-camps-SAH10-PDE4A1 (and Epac1-camps-SAH30-PDE4A1) the SAH10 (and SAH30) linkers were PCR amplified from plasmids encoding *systematic protein affinity strength modulation* (SPASM) sensors published previously (Sivaramakrishnan and Spudich, 2011), and BamHI and AscI restriction sites were introduced using the following set of primers (SAH10: #1: 5'-AAAAAAGGATCCGGAGAAGAGGAAGAGAAA-3', #2: 5'-AAAAAAGGCGCGCCAGAGCCCTTCTTCTTGCGTTTTTC-3', priming sequence underlined, restriction sites in italics; SAH30: #3: 5'-AAAAAAGGATCCGGAGAAGAGGAAGAGAAGAAG-3', #4: 5'-AAAAAAGGCGCGCCAGAGCCCTTTGTTTTCTTTCTGC-3'). PCR fragments were cut

with BamHI and AscI and cloned in frame between Epac1-camps and PDE4A1 using a variant of Epac1-camps-PDE4A1 (Herget et al., 2008) as vector. To generate Epac1-camps-PDE2A3, Epac1-camps-PDE2cat (amino acids 578-941 from PDE2A3), and Epac1-camps-SAH30-PDE2cat, the coding sequences of PDE2A3 and PDE2cat were PCR amplified and AscI and NotI restriction sites were inserted by using the following set of primers, respectively (PDE2A3: #5: 5'-AAAAAAAGGCGCGCCGGGCAGGCATGCGGCCAC-3', #6: 5'-AAAAAAGCGGCGCTCACTCAGCATCAAGGCT-3'; and PDE2cat: #7: 5'-AAAAAAAGGCGCGCTCCGACGATGAGTATACCAAACCTT-3', #8). The respective PCR products were cut with AscI and NotI and cloned in frame into Epac1-camps-PDE4A1 and Epac1-camps-SAH30-PDE4A1 where the PDE4A1 sequence was cut out with AscI and NotI. All constructs derived by restriction enzyme cloning were transformed and amplified in XL1-Blue competent E.coli (Agilent Technologies, Waldbronn, Germany).

AKAR4-PDE4A1 and AKAR4-PDE2A3 were generated by Gibson assembly using Epac1-camps-PDE4A1 and Epac1-camps-PDE2A3, respectively, as templates (Gibson et al., 2009). To generate AKAR4-PDE4A1, AKAR4 was PCR amplified using a pair of primers (#8: 5'-CTCACTATAGGGAGACCCAAGCTTTAAGGATCCCATGGTGAGCAAGGG-3', #9: 5'-CACCAAGGGCATGGATCCCTCGATGTTGTGGCGGATCTT-3') and inserted upstream of PDE4A1 in its vector which was linearized with the following primers (#10: 5'-AAGATCCGCCACAACATCGAGGGATCCATGCCCTTGGTG-3', #11: 5'-CCCTTGCTCACCATGGGATCCTTAAGCTTGGGTCTCCCTATAGTGAG-3'). To generate AKAR4-PDE2A3, AKAR4 was PCR amplified using another pair of primers (#12: 5'-GGGAGACCCAAGCTTAAGGATCCCATGGTGAGCAAG-3', #13: 5'-GCCGCATGCCTGCCC GCGCGCCTCTCGATGTTGTGGCGGAT-3') and inserted upstream

of PDE2A3 in its vector which was linearized with the following primers (#14: 5'-ATCCGCCACAACATCGAGAGGCGCGCCGGGCAGGCATGCGGC-3', #15: 5'-CTTGCTACCATGGGATCCTTAAGCTTGGGTCTCCCTAT-3').

To generate Epac1-camps-IRES2-PDE4A1, the IRES2 sequence was PCR amplified with the indicated primers (#16: 5'-GACGAGCTGTACAAGTGAGGATCCGCCCTCTCCCTCCCCCCCCCTA-3', #17: 5'-GCAGAAGAAATCCACCAAGGGCATGTGGCCATATTATCATCGTGTTT-3') and

inserted in frame in between Epac1-camps and PDE4A1 in the construct Epac1-camps-PDE4A1 which was linearized with the following primers (#18: 5'-

AAACACGATGATAATATGGCCACAATGCCCTTGGTGGATTCTTCTGTC-3', #19: 5'-TAGGGGGGGGGGAGGGAGAGGGGCGGATCCTCACTTGTACAGCTCGTC-3'. Epac1-

camps-IRES-PDE2cat was generated following exactly the same strategy using the following primers (IRES2:#20: 5'-

GACGAGCTGTACAAGTGAGGATCCAGGCGCGCCGCCCTCTCCCTCCCCCCCCCTA-3', #21: 5'-

AAGTTTGGTATACTCATCGTCGGACATGTGGCCATATTATCATCGTGTTT-3'; and linearization of Epac1-camps-PDE2A3: #22: 5'-

AAACACGATGATAATATGGCCACAATGTCCGACGATGAGTATAACAACTT-3', #23: 5'-

TAGGGGGGGGGGAGGGAGAGGGGCGGCGCCTGGATCCTCACTTGTACAGCTCGTC-3'). For assembly of the PCR products the Gibson Assembly® Master Mix (New England Biolabs GmbH, Frankfurt, Germany) was used according to the manufacturer's instructions. All

constructs derived by Gibson cloning were transformed and amplified in NEB® 5-alpha Competent

E.coli (New England Biolabs GmbH, Frankfurt, Germany).

All sequences were validated by automated sequencing of each construct by Eurofins (Luxembourg, Luxembourg) or LGC (Teddington, UK). Confocal images of HEK293 cells expressing all FRET-based constructs are compiled in **Figure S5**.

#### *8-FDA-cAMP cell penetration assays*

8-FDA-cAMP and FDA cell penetration assays were performed using a 96-well plate reader (Neo2, Biotek, Bad Friedrichshall, Germany), measuring whole fluorescence emission per well at 505 nm upon 488 nm excitation. 50,000 cells/well were seeded, and 24 wells were measured, in three replicates, for each experimental condition. Cells were kept in HBSS buffer, where spontaneous conversion of FDA and 8-FDA-cAMP to their fluorescent form is negligible. Confocal images of HEK293 cells loaded with either FDA or 8-FDA-cAMP are found in **Figure S2B-C**.

#### *Calibration compounds for diffusion measurements*

Fluorescein-labeled compounds of different molecular weight (fluorescein isothiocyanate-dextran of 20, 70kDa, and 250 kDa) were dissolved in water, and the pH was set to pH=9 by addition of NaOH. To pre-activate FDA into fluorescein, ester bonds in FDA were broken by incubation at 37°C for 30 minutes at pH 9. Concentrations were determined by absorbance spectroscopy in a ThermoFisher Evolution300 spectrophotometer. Measurements were performed at a final compound concentration of 100 nM. Approximately 40 µL of solution were inserted into an imaging chamber formed by a #1.5 coverslip immobilized onto a glass slide by melting two parallel stripes of Parafilm (Bemis Company, Neenah, USA).

### *Collecting linescans in a confocal microscope*

Linescans were acquired in a Leica SP8 confocal microscope (Leica Microsystems, Wetzlar, Germany), with a resonant scan head allowing 12 kHz line rate. Excitation was achieved using a white light laser, at the wavelengths of 488 nm. Excitation power was set to 10% of the maximal laser output (0.3 mW at 488 nm), and  $2 \cdot 10^6$  lines were collected within the sample, with a length of 256 pixels and a pixel size of 50 nm. A 40x 1.4 NA objective was used. Detection was performed in photon counting mode using Leica hybrid detectors. For 8-FDA-cAMP linescan experiments cells were plated on 25 mm (#1.5) coverslips and loaded for 30 minutes with 100 nM 8-FDA-cAMP at 37°C. Cells were then washed three times in Hank's Balanced Salt Solution (HBSS) (Thermofisher) and imaged in HBSS.

### *Extracting molecular diffusion*

Statistical analysis of the fluorescence fluctuations present in a sequence of images or a kymograph allows constructing a spatial-temporal correlation plot, containing the average single molecule transit times between any two arbitrary positions along the scan line (Ries et al., 2009, Hebert et al., 2005, Di Rienzo et al., 2013, Di Rienzo and Annibale, 2016). Such two-dimensional plots, namely Spatial-Temporal Image Correlation Spectroscopy (STICS) functions have two axes: a space and a time axis. The overall shape of the STICS function for diffusion is that of a 'plume', broadening in space as a function of time (**Figures 1A, S1A, S1B and S1C**). This broadening reflects the process of diffusion: the probability of finding a Brownian particle which is found at  $x=0$  for time  $t=0$  is a normal distribution of increasing variance as time elapses. The more rapid the broadening of the plume (**Figures S1A, S1B, and S1C**), the more rapid the molecular diffusion process. Horizontal sections of the plot provide Mean Squared Displacement (MSD) information

(i.e. broadening as a function of time) (**Figure S1D**). Vertical cross sections, known as average Pair Correlation functions, reflect the distribution of molecular transit times across a defined distance  $d$  (**Figure S1G**). These reflect the probability of finding a molecule at a given distance from its original position at time 0, after a time lag  $t$ . The position of the peak, reflecting the broadening of the STICS function, shifts to longer times as the diffusion coefficient decreases.

The temporal resolution of the measurement is determined by how rapidly the subsequent acquisitions of the same area (or line) are performed. In our setup, taking advantage of resonant scanners operating at 12 kHz, we could reach a temporal resolution of about 80  $\mu\text{s}$ .

Determining faster ( $> 100 \mu\text{m}^2/\text{s}$ ) diffusion is at the limit of this method, but it was possible to observe a convergence to previously measured cAMP diffusion values, viz.  $135 \pm 20 \mu\text{m}^2/\text{s}$ , by fitting progressively shorter time-lags. Furthermore, the distribution of rapid arrival times (**Figure S2G**) in forskolin/IBMX-stimulated cells further confirms the presence of a fast-moving component upon displacement, in the form of a peak at about 5 ms travel time over one  $\mu\text{m}$ .

#### *Model fitting to STICS functions*

Briefly, the  $256 \times 2 \cdot 10^6$  kymograph is corrected for drifts and slow fluctuations using a random number addition detrending, within a moving window of approximately  $250 \cdot 10^3$  lines, which corresponds to about 20 s. The fast Fourier transform (FFT) and its complex conjugate were then calculated, and their product was inverse FFTed to yield the autocorrelation function of the kymograph, namely the STICS function. We used a custom algorithm written in IGOR Pro (WaveMetrics), as previously described (Serfling et al., 2019, Di Rienzo and Annibale, 2016). For pure diffusion, the equation describing the STICS Function reads as follows (Ries et al., 2009):



$$G(x, t) = \frac{\gamma}{(N \cdot D \cdot t + \sigma_0^2)} e^{-\left(\frac{t^2 + (x-x_0)^2}{(4 \cdot D \cdot t + \sigma_0^2)}\right)}$$

### Equation 1

With  $x$  and  $t$  being space and time, respectively, and  $\gamma$  the so-called gamma factor of the Point Spread Function (PSF) of the microscope, normally 0.35.  $N$  is the number of fluorescent molecules in the PSF,  $D$  the diffusion coefficient of the species and  $\sigma_0$  the waist of the PSF (of the order of 250-300 nm for the wavelength used). For each given  $t$ , **eq. 1** can also be used for a line by line fit of the STICS function (as described in **Figures S1D**), yielding the MSDs reported in **Figure S1E**, as graphically highlighted in **Figure S1F**.

In the case of two species displaying distinct concentrations and diffusion rates, the equation becomes (with 1 and 2 referring to each of the two species, respectively):

$$G_2(x, t) = \frac{\gamma}{(N1 \cdot D1 \cdot t + \sigma_0^2)} e^{-\left(\frac{t^2 + (x-x_0)^2}{(4 \cdot D1 \cdot t + \sigma_0^2)}\right)} + \frac{\gamma}{(N2 \cdot D2 \cdot t + \sigma_0^2)} e^{-\left(\frac{t^2 + (x-x_0)^2}{(4 \cdot D2 \cdot t + \sigma_0^2)}\right)}$$

### Equation 2

#### *Interpretation of MSD at multiple timescales*

When two species with distinct diffusion coefficients combine, e.g. a fast diffusing and a slow diffusing component/bound component, a fast broadening STICS function and a slow one overlap. **Figure S2H and S2I** illustrate how this reflects in terms of the measured STICS function and recovered MSD, respectively: a first rapid increase of MSD is followed by a decrease and again an increase, although at a slow pace. This should be interpreted in the following way: when the temporal resolution of the sampling is high enough, e.g. less than 10 ms as in **Figure S2I**, then rapid ‘jumps’ of the molecules can be appreciated. However, once the temporal resolution is lower, e.g. above 100 ms, then the fast jumps cannot be captured anymore, and we are in the domain

where the slower diffusing species dominates the MSD. This simulated plot represents the scenario observed in **Figure 1** for the fsk/IBMX stimulated cells, where a fraction of the 8-F-cAMP diffuses very rapidly, on the background of a major fraction that still moves very slowly.

#### *Single-cell FRET measurements*

Transfected HEK293 cells were transferred to imaging chambers (Attofluor™, ThermoFisher Scientific), washed twice with FRET imaging buffer (144 mM NaCl, 5.4 mM KCl, 2 mM CaCl<sub>2</sub> (Carl Roth GmbH & Co. KG, Karlsruhe, Germany), 1 mM MgCl<sub>2</sub> (AppliChem, Darmstadt, Germany), 10 mM HEPES (Sigma-Aldrich Chemie GmbH); pH = 7.3). FRET measurements were carried out at room temperature using an epifluorescence microscope (Leica DMI8 inverted microscope, Leica Microsystems, Wetzlar, Germany) equipped with an oil immersion objective (HC PL APO 40x/1.30, Leica Microsystems, Wetzlar, Germany), a dichroic beam splitter (T505lpxr, Visitron Systems, Puchheim, Germany), a high-speed polychromator (VisiChrome, Visitron Systems), a Xe-Lamp (75W, 5.7 A, Hamamatsu Photonics, Hamamatsu City, Japan), a camera system (Photometrics Prime 95B CMOS camera, Visitron systems) with an Optosplit II dual emission image splitter (Cairn, Edinburgh, Scotland, UK) with CFP 470/24 and YFP 535/30 emission filters (Chroma Technology, Bellows Falls, VT, USA). Cells were brought into focus and regions of interest were drawn around single cells using the VisiView® 4.0 imaging software (Visitron Systems). Spatial homogeneity of the expression of the constructs was taken into account by ROI selection. In general, large ROIs containing most of the cell allow for averaging out any residual spatial heterogeneity within the cytosol. A time series of images was recorded every 5 seconds upon 100 ms exposure to 436 nm light. After reaching a stable baseline, cells were stimulated with the β-adrenergic agonist isoproterenol (Iso, 10 μM), followed by specific PDE inhibition (300 nM roflumilast for PDE4A1 constructs, and 100 nM BAY 60-7550 for PDE2cat

and PDE2A3 constructs). To reach maximal cAMP levels, a combination of forskolin (10  $\mu$ M) and IBMX (100  $\mu$ M) were applied at the end of every experiment. Data from individual channels (CFP and YFP) were exported and corrected offline for background and bleedthrough (Borner et al., 2011). Inverted FRET ratios (CFP/FRET) were calculated and normalized to baseline (average of 10 data points before compound addition, set to 0% and forskolin/IBMX (max cAMP response, set to 100 %). After every experiment, direct YFP excitation at 505 nm (emission: 560 nm) was recorded to evaluate expression levels of the sensors.

#### *FRET measurements in cytosolic preparations*

Transfected HEK293 cells on a 10 cm plate (corresponding to approximately  $1-1.5 \times 10^7$  cells) were washed twice with ice-cold Dulbecco's Phosphate Buffered Saline (Sigma-Aldrich) and harvested in 300  $\mu$ L lysis buffer (10 mM Tris-HCl, 10 mM MgCl<sub>2</sub>, pH 7.4) containing 1 mM PMSF and protease inhibitors (20  $\mu$ g/mL trypsin inhibitor from soybean and 60  $\mu$ g/mL benzamide). Cells were lysed by homogenization (two rounds of 10 s each using an T8 Ultra-Turrax® homogenizer (IKA, Staufen, Germany)). Nuclei and cell debris were spun down by centrifugation (1000xg, 5 min, 4°C). To obtain the cytosolic fraction, the supernatant was centrifuged again (100.000xg, 30 min, 4°C). The resultant supernatants were transferred to a quartz cuvette and adjusted with 10 mM Tris-HCl, 10 mM MgCl<sub>2</sub> (pH 7.4) to comparable sensor densities (assessed by direct YFP excitation). Fluorescence emission spectra were recorded with a LS50B spectrometer (PerkinElmer Life Sciences, Waltham, MA, USA) at 436 nm excitation, and emission was measured between 460 and 550 nm after adding increasing concentrations of cAMP. 480/525 nm FRET emission ratios were calculated at different cAMP concentrations and fitted with a three-parameter logistic function and normalized to the lower (absence of cAMP; set 0%) and upper plateau (saturating concentrations of cAMP, set 100%) of the concentration-effect curves.

### *Quantification of cAMP binding sites*

Cytosolic HEK293 cell preparations for the quantification of buffering capacities (**Figure S4**) were prepared as follows: HEK293 cells grown on a 10 cm dish, containing approximately  $1 \times 10^7$  cells, were harvested in 300  $\mu\text{L}$  binding buffer (20 mM MOPS, 150 mM NaCl, 0.005% CHAPS, pH7) containing 1mM PMSF and protease inhibitors (20  $\mu\text{g}/\text{mL}$  trypsin inhibitor from soybean and 60  $\mu\text{g}/\text{mL}$  benzamidine) and cytosolic extracts were prepared according to the protocol described above (*FRET measurements in cytosolic preparations*). Estimating an average cell volume of 1 pL per cell, the total cell volume of harvested cells (10  $\mu\text{L}$ ) is diluted 30 times (30x) by addition of 300  $\mu\text{L}$  binding buffer for harvesting. For anisotropy measurements, 0.5 mM IBMX were added and the cytosolic preparation was further diluted twice or 50 times with binding buffer, resulting in a 60x or 1500x, respectively. Steady state anisotropy (from here on only referred to as ‘anisotropy’) as well as fluorescence excitation and emission spectra were measured on a Horiba Yobin-Yvon Fluoromax Plus spectrophotometer using the appropriate routine of the FluorEssence software. 8-F-cAMP and fluorescein were both excited at 485 nm and fluorescence was measured at 535 nm. Slit width was 5 nm for both excitation and emission. 600  $\mu\text{L}$  of solution were pipetted in a quartz Cuvette (Thorlabs). Integration time was set to between 1-10 s. Fluorescence intensity  $I$  was measured along all polarizations ( $I_{hh}$ ,  $I_{hv}$ ,  $I_{vv}$ ,  $I_{vh}$ ) and anisotropy  $r$  was calculated according to the standard equation (Jameson and Ross, 2010):

$$r = \frac{\frac{I_{hh}I_{hh} - 1}{I_{hv}I_{vh}}}{\frac{I_{hh}I_{hh} + 2}{I_{hv}I_{vh}}}$$

### **Equation 3**

When imaging scattering solutions (such as cytosolic cell extracts) anisotropy values were corrected to those of the pure solution - without any fluorescent dye added - by subtracting each of the corresponding fluorescence intensity values at each polarization.

### *Molecular brightness*

Molecular brightness experiments were performed as previously reported (Annibale and Lohse, 2020). Briefly, movies of 100 frames of individual cells were acquired using a Laser Scanning Confocal Microscope SP8 (Leica), at a speed of 400 Hz, with an excitation power of 3% at 514 nm, corresponding to a few  $\mu\text{W}$  in the sample plane. Detection was performed using photon counting detectors (Leica HyD), in the spectral range 520-600 nm. Molecular brightness values per pixel dwell time were calculated for each pixel, and the average cytosolic value from each individual cell is reported, after converting to photon counts/s. Briefly, molecular brightness is calculated by measuring the variance  $\sigma$  of the photon counts over time for each pixel by the average intensity value  $k$ , according to the formula:  $\sigma^2/k$ . The values of all the pixel within a homogeneous area of the cytosol are then averaged together.

### *Confocal microscopy*

Fluorescence microscopy experiments were performed either on a Leica SP8 Confocal Microscopes, using HyD photon counting detectors and a White Laser light source to achieve excitation at the desired wavelengths (488 nm, and 514 nm). Emission was collected in the 500-600 nm and 520-600 nm range respectively. A 40x 1.3 NA objective was used, and the electronic zoom was set to achieve a pixel size of 50 nm.

### *Biophysical model of cAMP signaling at the nanoscale*

We have modeled cAMP reaction/diffusion behavior in the cell, in particular in the vicinity of a PDE, according to the classical treatment original provided by Smoluchowski (Smoluchowski, 1916) (details in **Methods S2**). Here, the catalytic site of the PDE is seen as a sphere of radius  $R$  and cAMP as a species diffusing (with a diffusion coefficient  $D$ ) in its vicinity, assuming that no cAMP sources are close by. The notion that the diffusion is buffered affects the free cAMP

concentration [cAMP], and in all our calculations the diffusion coefficient D refers to the free cAMP diffusion rate. This assumption is justified as we are interested in length scales of the order 30 nm, which is well below the average distance between two PDEs at physiological concentrations. Once the cAMP reaches the surfaces of the sphere, a degradation reaction takes place, making the PDE effectively a spherical sink characterized by a flux I of molecules degraded per unit time, in units of mol/s (or nmol/s or  $\mu\text{mol/s}$ ). The requirement that the total flux of free cAMP towards the PDE at the radius R equals the turnover I (Rice, 1985), leads to the relation

$$4\pi R^2 D \left. \frac{\partial [\text{cAMP}]}{\partial r} \right|_{r=R} = I. \text{ Equation 4}$$

Field Code Changed

Which allows to solve the appropriate reaction-diffusion equation in spherical coordinates, leading to the following relation for [cAMP] as a function of the distance r from the PDE

$$[\text{cAMP}](r) = [\text{cAMP}]_{\text{bulk}} - \frac{I}{4\pi D r}. \text{ Equation 5}$$

Field Code Changed

The equation can also be written in terms of the radius  $R_0$  where the concentration would be 0, i.e. the radius of a perfect absorber.

$$[\text{cAMP}](r) = [\text{cAMP}]_{\text{bulk}} \left( 1 - \frac{R_0}{r} \right). \text{ Equation 6}$$

Field Code Changed

## QUANTIFICATION AND STATISTICAL ANALYSIS

Data analysis was performed using GraphPad Prism software 7.0 (GraphPad Software, San Diego, USA) and Igor Pro 7 (Wavemetrics, Lake Oswego, USA). Normal distribution of data points was tested in every data set using D'Agostino-Pearson omnibus normality test before evaluating significance. When comparing two populations, a Student's t-test was used. When comparing three or more populations, a parametric one-way ANOVA with Tukey's multiple comparison test was used. The confidence interval was set to 95% (p-value = 0.05). Significance was assessed as

followed: ns (not significant) \*:  $p \leq 0.05$ ; \*\*:  $p \leq 0.01$ ; \*\*\*:  $p \leq 0.001$ , \*\*\*\*:  $p \leq 0.0001$ . Data are represented throughout as mean  $\pm$  error (s.e.m., SD, or 95% confidence intervals), plus – where appropriate – as scatter plots of individual results. More details about statistics, e.g. repetition of experiments and cell numbers, are indicated in the respective figure legends.

## REFERENCES:

- AGARWAL, S. R., CLANCY, C. E. & HARVEY, R. D. 2016. Mechanisms Restricting Diffusion of Intracellular cAMP. *Sci Rep*, 6, 19577.
- ANNIBALE, P. & LOHSE, M. J. 2020. Spatial heterogeneity in molecular brightness. *Nat Methods*, 17, 273-275.
- ARRIO-DUPONT, M., CRIBIER, S., FOUCAULT, G., DEVAUX, P. F. & D'ALBIS, A. 1996. Diffusion of fluorescently labeled macromolecules in cultured muscle cells. *Biophys J*, 70, 2327-32.
- BACSKAI, B. J., HOCHNER, B., MAHAUT-SMITH, M., ADAMS, S. R., KAANG, B. K., KANDEL, E. R. & TSIEN, R. Y. 1993. Spatially resolved dynamics of cAMP and protein kinase A subunits in Aplysia sensory neurons. *Science*, 260, 222-6.
- BATHE-PETERS, M., GMACH, P., ANNIBALE, P. & LOHSE, M. J. 2020. Linescan microscopy data to extract diffusion coefficient of a fluorescent species using a commercial confocal microscope. *Data Brief*, 29, 105063.
- BENDER, A. T. & BEAVO, J. A. 2006. Cyclic nucleotide phosphodiesterases: molecular regulation to clinical use. *Pharmacol Rev*, 58, 488-520.
- BORNER, S., SCHWEDE, F., SCHLIPP, A., BERISHA, F., CALEBIRO, D., LOHSE, M. J. & NIKOLAEV, V. O. 2011. FRET measurements of intracellular cAMP concentrations and cAMP analog permeability in intact cells. *Nat Protoc*, 6, 427-38.
- BRUNTON, L. L., HAYES, J. S. & MAYER, S. E. 1979. Hormonally specific phosphorylation of cardiac troponin I and activation of glycogen phosphorylase. *Nature*, 280, 78-80.
- BUXTON, I. L. & BRUNTON, L. L. 1983. Compartments of cyclic AMP and protein kinase in mammalian cardiomyocytes. *J Biol Chem*, 258, 10233-9.
- CHEN, C., NAKAMURA, T. & KOUTALOS, Y. 1999. Cyclic AMP diffusion coefficient in frog olfactory cilia. *Biophys J*, 76, 2861-7.
- CONTI, M. & BEAVO, J. 2007. Biochemistry and physiology of cyclic nucleotide phosphodiesterases: essential components in cyclic nucleotide signaling. *Annu Rev Biochem*, 76, 481-511.
- CORBIN, J. D., SUGDEN, P. H., LINCOLN, T. M. & KEELY, S. L. 1977. Compartmentalization of adenosine 3':5'-monophosphate and adenosine 3':5'-monophosphate-dependent protein kinase in heart tissue. *J Biol Chem*, 252, 3854-61.



- DEPRY, C., ALLEN, M. D. & ZHANG, J. 2011. Visualization of PKA activity in plasma membrane microdomains. *Mol Biosyst*, 7, 52-8.
- DI RIENZO, C. & ANNIBALE, P. 2016. Visualizing the molecular mode of motion from a correlative analysis of localization microscopy datasets. *Opt Lett*, 41, 4503-4506.
- DI RIENZO, C., GRATTON, E., BELTRAM, F. & CARDARELLI, F. 2013. Fast spatiotemporal correlation spectroscopy to determine protein lateral diffusion laws in live cell membranes. *Proceedings of the National Academy of Sciences of the United States of America*, 110, 12307-12312.
- FEINSTEIN, W. P., ZHU, B., LEAVESLEY, S. J., SAYNER, S. L. & RICH, T. C. 2012. Assessment of cellular mechanisms contributing to cAMP compartmentalization in pulmonary microvascular endothelial cells. *Am J Physiol Cell Physiol*, 302, C839-52.
- GIBSON, D. G., YOUNG, L., CHUANG, R. Y., VENTER, J. C., HUTCHISON, C. A., 3RD & SMITH, H. O. 2009. Enzymatic assembly of DNA molecules up to several hundred kilobases. *Nat Methods*, 6, 343-5.
- GOLD, M. G., GONEN, T. & SCOTT, J. D. 2013. Local cAMP signaling in disease at a glance. *J Cell Sci*, 126, 4537-43.
- HAYES, J. S., BRUNTON, L. L. & MAYER, S. E. 1980. Selective activation of particulate cAMP-dependent protein kinase by isoproterenol and prostaglandin E1. *J Biol Chem*, 255, 5113-9.
- HEBERT, B., COSTANTINO, S. & WISEMAN, P. W. 2005. Spatiotemporal image correlation spectroscopy (STICS) theory, verification, and application to protein velocity mapping in living CHO cells. *Biophys J*, 88, 3601-14.
- HERGET, S., LOHSE, M. J. & NIKOLAEV, V. O. 2008. Real-time monitoring of phosphodiesterase inhibition in intact cells. *Cell Signal*, 20, 1423-31.
- HOUSLAY, M. D. 2010. Underpinning compartmentalised cAMP signalling through targeted cAMP breakdown. *Trends Biochem Sci*, 35, 91-100.
- HUANG, R. C. & GILLETTE, R. 1993. Co-regulation of cAMP-activated Na<sup>+</sup> current by Ca<sup>2+</sup> in neurones of the mollusc Pleurobranchaea. *J Physiol*, 462, 307-20.
- JAMESON, D. M. & ROSS, J. A. 2010. Fluorescence polarization/anisotropy in diagnostics and imaging. *Chem Rev*, 110, 2685-708.

- LOHSE, C., BOCK, A., MAIELLARO, I., HANNAWACKER, A., SCHAD, L. R., LOHSE, M. J. & BAUER, W. R. 2017. Experimental and mathematical analysis of cAMP nanodomains. *PLoS One*, 12, e0174856.
- MIKA, D., LEROY, J., VANDECASTEELE, G. & FISCHMEISTER, R. 2012. PDEs create local domains of cAMP signaling. *J Mol Cell Cardiol*, 52, 323-9.
- MO, G. C., ROSS, B., HERTEL, F., MANNA, P., YANG, X., GREENWALD, E., BOOTH, C., PLUMMER, A. M., TENNER, B., CHEN, Z., WANG, Y., KENNEDY, E. J., COLE, P. A., FLEMING, K. G., PALMER, A., JIMENEZ, R., XIAO, J., DEDECKER, P. & ZHANG, J. 2017. Genetically encoded biosensors for visualizing live-cell biochemical activity at super-resolution. *Nat Methods*, 14, 427-434.
- NIKOLAEV, V. O., BUNEMANN, M., HEIN, L., HANNAWACKER, A. & LOHSE, M. J. 2004. Novel single chain cAMP sensors for receptor-induced signal propagation. *J Biol Chem*, 279, 37215-8.
- NIKOLAEV, V. O., BUNEMANN, M., SCHMITTECKERT, E., LOHSE, M. J. & ENGELHARDT, S. 2006. Cyclic AMP imaging in adult cardiac myocytes reveals far-reaching beta1-adrenergic but locally confined beta2-adrenergic receptor-mediated signaling. *Circ Res*, 99, 1084-91.
- NIKOLAEV, V. O., GAMBARYAN, S., ENGELHARDT, S., WALTER, U. & LOHSE, M. J. 2005. Real-time monitoring of the PDE2 activity of live cells: hormone-stimulated cAMP hydrolysis is faster than hormone-stimulated cAMP synthesis. *J Biol Chem*, 280, 1716-9.
- NIKOLAEV, V. O., MOSHKOV, A., LYON, A. R., MIRAGOLI, M., NOVAK, P., PAUR, H., LOHSE, M. J., KORCHEV, Y. E., HARDING, S. E. & GORELIK, J. 2010. Beta2-adrenergic receptor redistribution in heart failure changes cAMP compartmentation. *Science*, 327, 1653-7.
- OMORI, K. & KOTERA, J. 2007. Overview of PDEs and their regulation. *Circ Res*, 100, 309-27.
- PANDIT, J., FORMAN, M. D., FENNELL, K. F., DILLMAN, K. S. & MENNITI, F. S. 2009. Mechanism for the allosteric regulation of phosphodiesterase 2A deduced from the X-ray structure of a near full-length construct. *Proc Natl Acad Sci U S A*, 106, 18225-30.
- PERERA, R. K. & NIKOLAEV, V. O. 2013. Compartmentation of cAMP signalling in cardiomyocytes in health and disease. *Acta Physiol (Oxf)*, 207, 650-62.

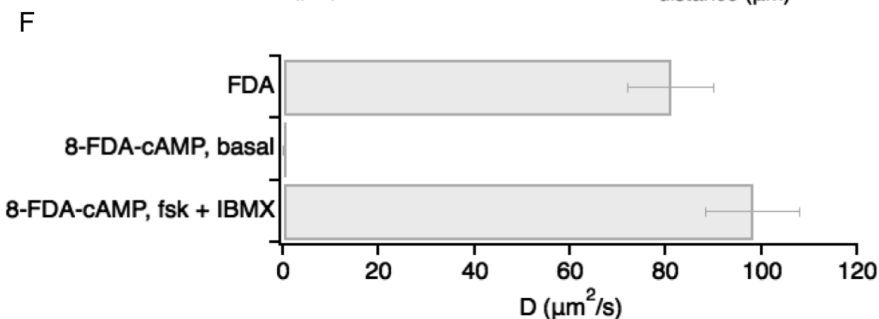
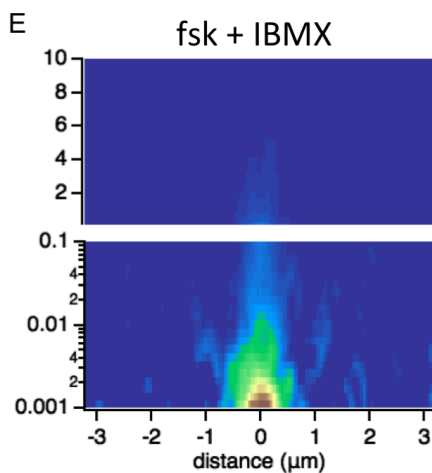
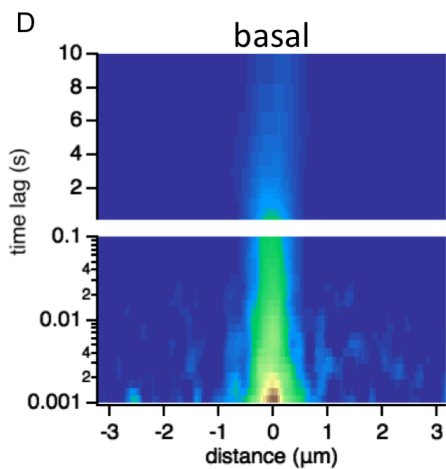
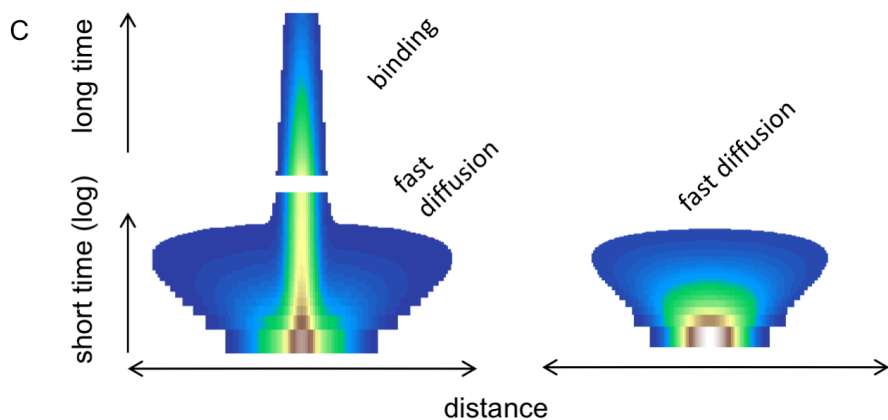
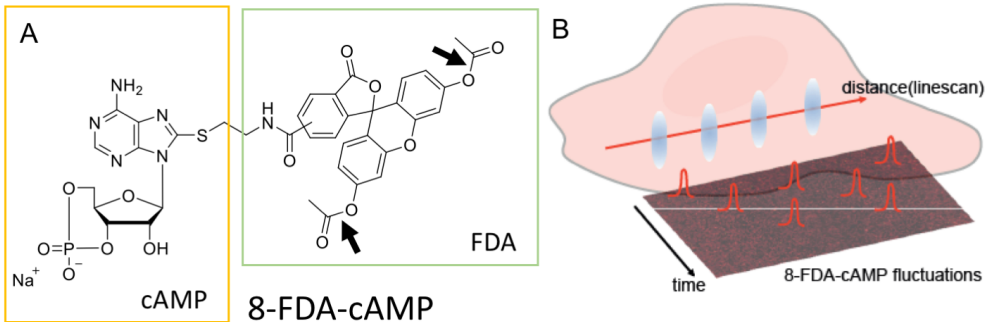
- RICE, S. A. 1985. *Diffusion-Limited Reactions. Comprehensive Chemical Kinetics*, Elsevier.
- RICH, T. C., FAGAN, K. A., NAKATA, H., SCHAACK, J., COOPER, D. M. & KARPEN, J. W. 2000. Cyclic nucleotide-gated channels colocalize with adenylyl cyclase in regions of restricted cAMP diffusion. *J Gen Physiol*, 116, 147-61.
- RICH, T. C., FAGAN, K. A., TSE, T. E., SCHAACK, J., COOPER, D. M. & KARPEN, J. W. 2001. A uniform extracellular stimulus triggers distinct cAMP signals in different compartments of a simple cell. *Proc Natl Acad Sci U S A*, 98, 13049-54.
- RICHARDS, M., LOMAS, O., JALINK, K., FORD, K. L., VAUGHAN-JONES, R. D., LEFKIMMIATIS, K. & SWIETACH, P. 2016. Intracellular tortuosity underlies slow cAMP diffusion in adult ventricular myocytes. *Cardiovasc Res*, 110, 395-407.
- RIES, J., CHIANTIA, S. & SCHWILLE, P. 2009. Accurate determination of membrane dynamics with line-scan FCS. *Biophys J*, 96, 1999-2008.
- SERFLING, R., SEIDEL, L., BOCK, A., LOHSE, M. J., ANNIBALE, P. & COIN, I. 2019. Quantitative Single-Residue Bioorthogonal Labeling of G Protein-Coupled Receptors in Live Cells. *ACS Chem Biol*, 14, 1141-1149.
- SIVARAMAKRISHNAN, S. & SPUDICH, J. A. 2011. Systematic control of protein interaction using a modular ER/K alpha-helix linker. *Proc Natl Acad Sci U S A*, 108, 20467-72.
- SMITH, F. D., ESSELTINE, J. L., NYGREN, P. J., VEESLER, D., BYRNE, D. P., VONDERACH, M., STRASHNOV, I., EYERS, C. E., EYERS, P. A., LANGEBERG, L. K. & SCOTT, J. D. 2017. Local protein kinase A action proceeds through intact holoenzymes. *Science*, 356, 1288-1293.
- SMOLUCHOWSKI, M. V. 1916. Drei Vorträge über Diffusion, Brownsche Bewegung und Koagulation von Kolloidteilchen. *Physik. Zeit.*, 17, 557-571; 585-599.
- STANGHERLIN, A. & ZACCOLO, M. 2012. Phosphodiesterases and subcellular compartmentalized cAMP signaling in the cardiovascular system. *Am J Physiol Heart Circ Physiol*, 302, H379-90.
- TERRIN, A., DI BENEDETTO, G., PERTEGATO, V., CHEUNG, Y. F., BAILLIE, G., LYNCH, M. J., ELVASSORE, N., PRINZ, A., HERBERG, F. W., HOUSLAY, M. D. & ZACCOLO, M. 2006. PGE(1) stimulation of HEK293 cells generates multiple contiguous domains with different [cAMP]: role of compartmentalized phosphodiesterases. *J Cell Biol*, 175, 441-51.

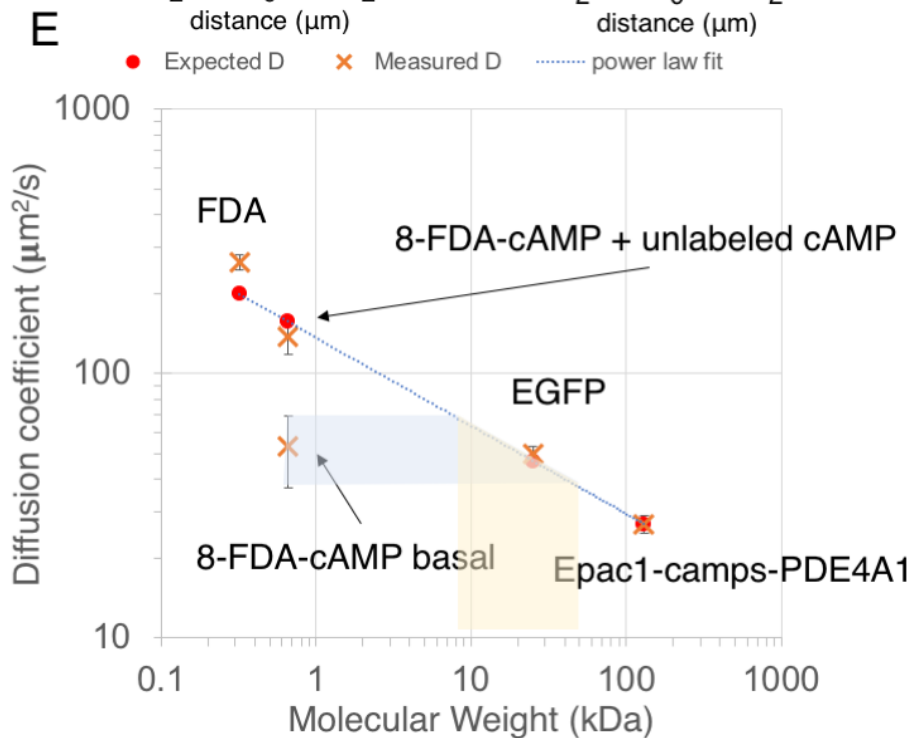
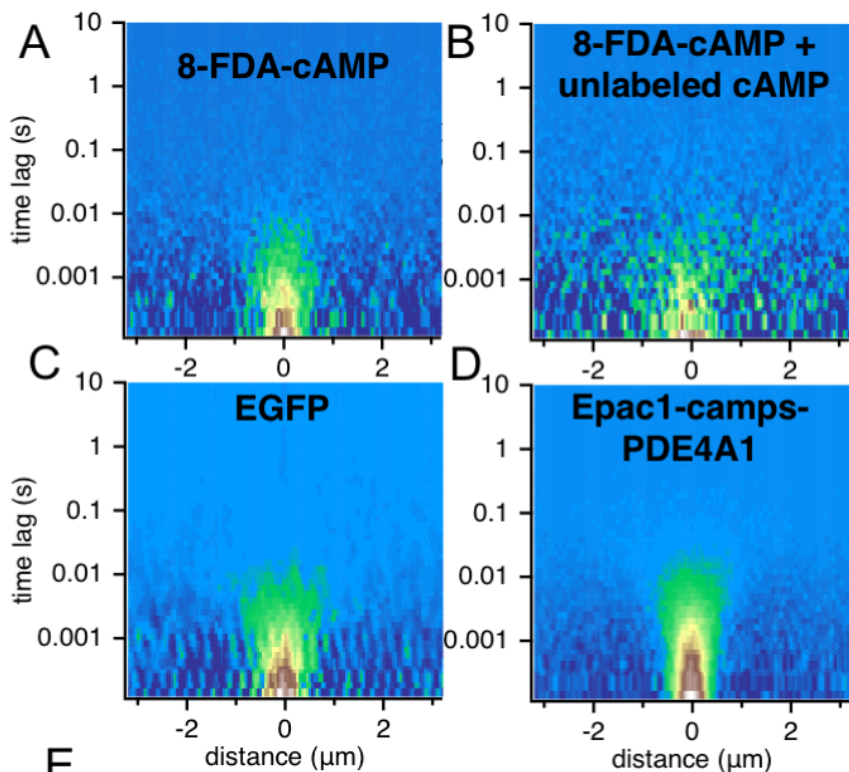
- WAGNER, J. & KEIZER, J. 1994. Effects of rapid buffers on Ca<sup>2+</sup> diffusion and Ca<sup>2+</sup> oscillations. *Biophys J*, 67, 447-56.
- WALKER-GRAY, R., STENGEL, F. & GOLD, M. G. 2017. Mechanisms for restraining cAMP-dependent protein kinase revealed by subunit quantitation and cross-linking approaches. *Proc Natl Acad Sci U S A*, 114, 10414-10419.
- XIN, W., FEINSTEIN, W. P., BRITAIN, A. L., OCHOA, C. D., ZHU, B., RICHTER, W., LEAVESLEY, S. J. & RICH, T. C. 2015. Estimating the magnitude of near-membrane PDE4 activity in living cells. *Am J Physiol Cell Physiol*, 309, C415-24.
- ZACCOLO, M. 2009. cAMP signal transduction in the heart: understanding spatial control for the development of novel therapeutic strategies. *Br J Pharmacol*, 158, 50-60.
- ZACCOLO, M. 2011. Spatial control of cAMP signalling in health and disease. *Curr Opin Pharmacol*, 11, 649-55.

## KEY RESOURCES TABLE

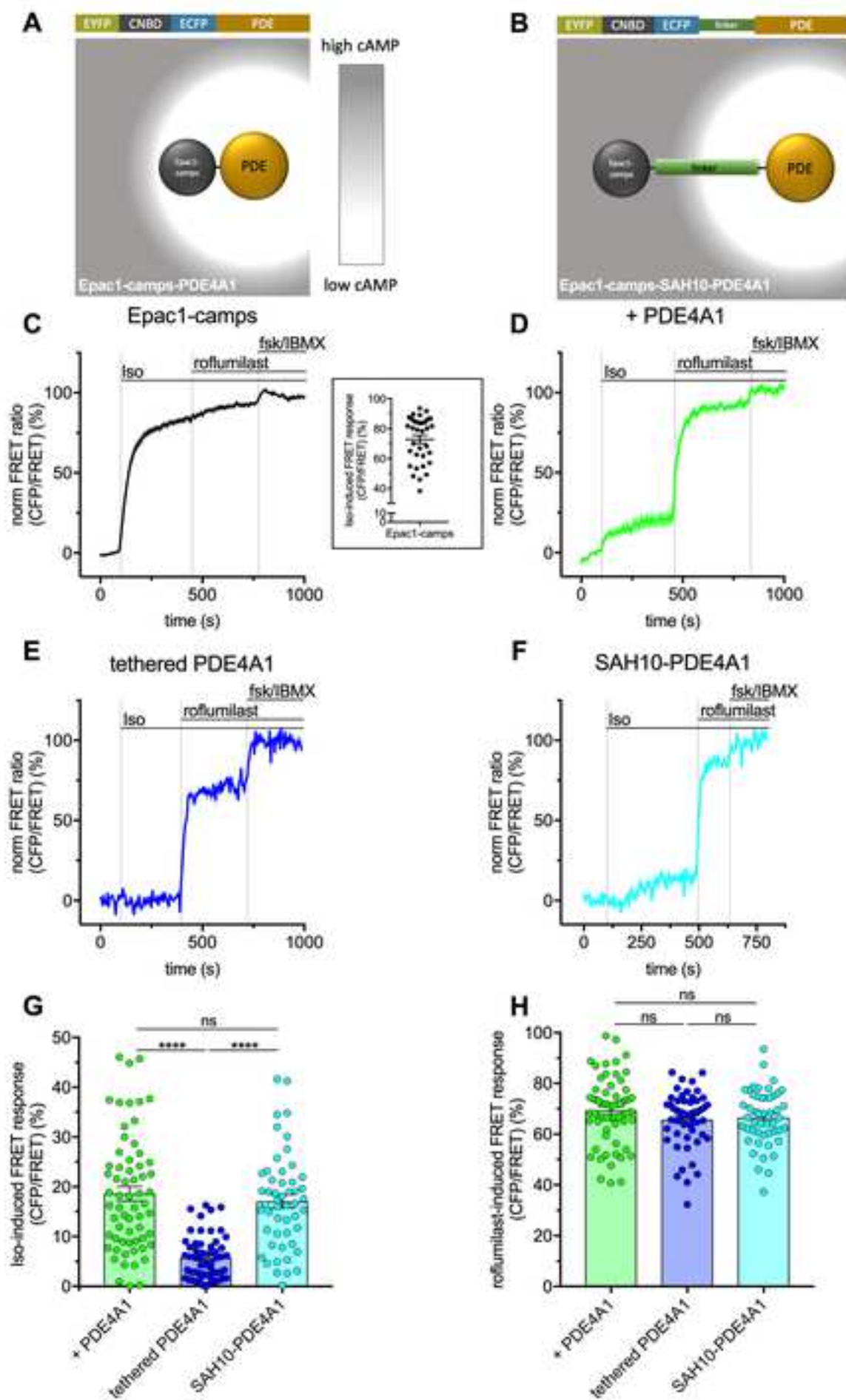
REAGENT or RESOURCE	SOURCE	IDENTIFIER
Bacterial and Virus Strains		
NEB® 5-alpha Competent E.coli (High Efficiency)	New England Biolabs	Cat#: C2987
XL1-Blue Competent Cells	Agilent	Cat#: 200249
Chemicals, Peptides, and Recombinant Proteins		
(-)-Isoproterenol hydrochloride	Sigma-Aldrich	Cat#: I6504; CAS: 5984-95-2
3-isobutyl-1-methylxanthin (IBMX)	Sigma-Aldrich	Cat#: I5879; CAS: 28822-58-4
8-FDA-cAMP	BIOLOG Life Science Institute	N/A
Adenosine 3',5'-cyclic monophosphate sodium salt monohydrate (cAMP)	Sigma-Aldrich	Cat#: A6885; CAS: 37839-81-9
BAY 60-7550	Cayman Chemical	Cat#: 10011135; CAS: 439083-90-6
Benzamidine	Sigma-Aldrich	Cat#: 12072; CAS: 618-39-3
CHAPS	Avanti Polar Lipids	Cat#: 850500P; CAS: 75621-03-3
Effectene Transfection Reagent	Qiagen	Cat#: 301427
Fluorescein	ThermoFisher Scientific	Cat#: 10700795; CAS: 2321-07-5
Fluorescein diacetate	Sigma-Aldrich	Cat#: F7378 CAS: 596-09-8
Fluorescein isothiocyanate-dextran 20 kDa	Sigma-Aldrich	Cat#: FD20; CAS: 60842-46-8
Fluorescein isothiocyanate-dextran 250 kDa	Sigma-Aldrich	Cat#: FD250S; CAS: 60842-46-8
Fluorescein isothiocyanate-dextran 70 kDa	Sigma-Aldrich	Cat#: 90718; CAS: 60842-46-8
Forskolin	BioTrend	Cat#: AOB6380-5; CAS: 66575-29-9
Gibson Assembly® Master Mix	New England Biolabs (Gibson et al., 2009)	Cat#: E2611
Phenylmethanesulfonyl fluoride (PMSF)	Sigma-Aldrich	Cat#: P7626; CAS: 329-98-6
Phosphodiesterase, 3',5'-cyclic-nucleotide-specific from bovine brain	Sigma-Aldrich	Cat#: P9529; CAS: 9040-59-9
Purified PKA R1alpha, human	Biaffin GmbH&co KG	Cat#: PK-PKA-R1A025
Roflumilast	Tocris Bioscience	Cat#: 6641; CAS: 162401-32-3
Trypsin inhibitor from soybean	Sigma-Aldrich	Cat#: T9003; CAS: 9035-81-8
Critical Commercial Assays		
PDELIGHT™ HTS cAMP Phosphodiesterase Assay Kit	Lonza	Cat#: LT07-600
PKA (Protein Kinase A) Colorimetric Activity Kit	ThermoFisher Scientific	Cat#: EIAPKA
Experimental Models: Cell Lines		

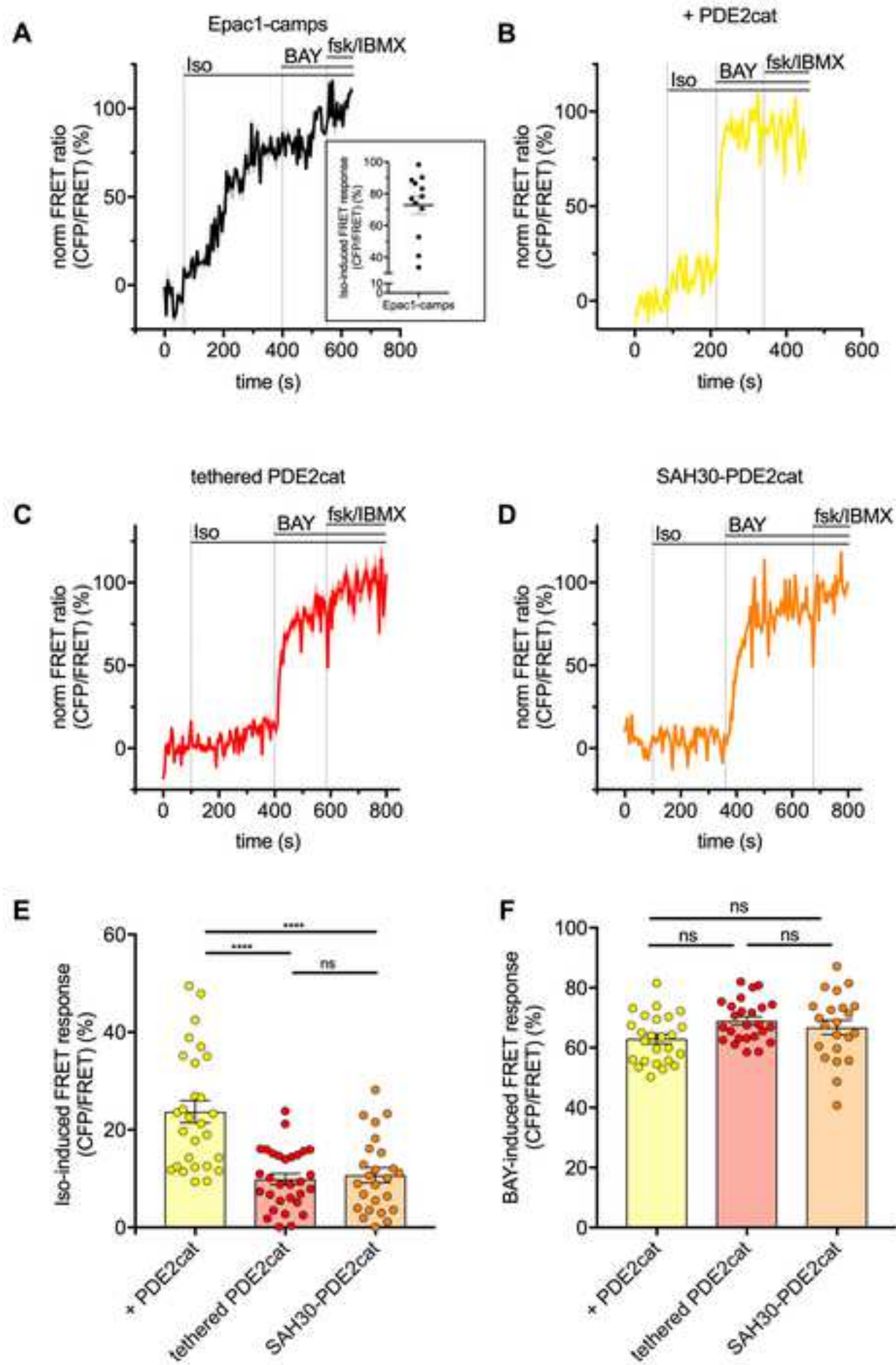
HEK-tsA201 cells	Sigma-Aldrich	ECACC Cat# 96121229
Oligonucleotides		
Primers for Cloning, see Table S2	This paper	N/A
Recombinant DNA		
PDE2A (NM_002599) Human Untagged Clone	OriGene Technologies	Cat#: SC110970
Epac1-camps	Nikolaev et al., 2004	N/A
Epac1-camps-PDE4A1	Herget et al., 2008	N/A
Epac1-camps-PDE4A1 D352A	Herget et al., 2008	N/A
Epac1-camps-SAH10-PDE4A1	This paper	N/A
Epac1-camps-IRES2-PDE4A1	This paper	N/A
Epac1-camps-PDE2A3	This paper	N/A
Epac1-camps-PDE2cat	This paper	N/A
Epac1-camps-SAH30-PDE2cat	This paper	N/A
Epac1-camps-IRES2-PDE2cat	This paper	N/A
pcDNA3-AKAR4	Dr. Jin Zhang (UC San Diego, USA) (Depry et al., 2011)	Addgene Plasmid #61619
AKAR4-PDE4A1	This paper	N/A
AKAR4-PDE2A3	This paper	N/A
SPASM sensor with 10 nm ERK $\alpha$ -helix	Sivaramakrishnan and Spudich, 2011	N/A
SPASM sensor with 30 nm ERK $\alpha$ -helix	Sivaramakrishnan and Spudich, 2011	N/A
Software and Algorithms		
GraphPad Prism software 7.0	GraphPad Software Inc.	<a href="https://www.graphpad.com/scientific-software/prism/">https://www.graphpad.com/scientific-software/prism/</a>
IGOR Pro 7	WaveMetrics	<a href="https://www.wavemetrics.com/products/igorpro">https://www.wavemetrics.com/products/igorpro</a>
Customs STICS code	Serfling et al., 2019 Bathe-Peters et al., 2020	available upon request to the authors
FluorEssence™	Horiba	<a href="https://www.horiba.com/en_en/products/detail/action/show/Product/fluorescence-1378/">https://www.horiba.com/en_en/products/detail/action/show/Product/fluorescence-1378/</a>
VisiView® 4.0 imaging software	Visitron Systems	<a href="https://www.visitron.de/products/visiview-r-software.html">https://www.visitron.de/products/visiview-r-software.html</a>

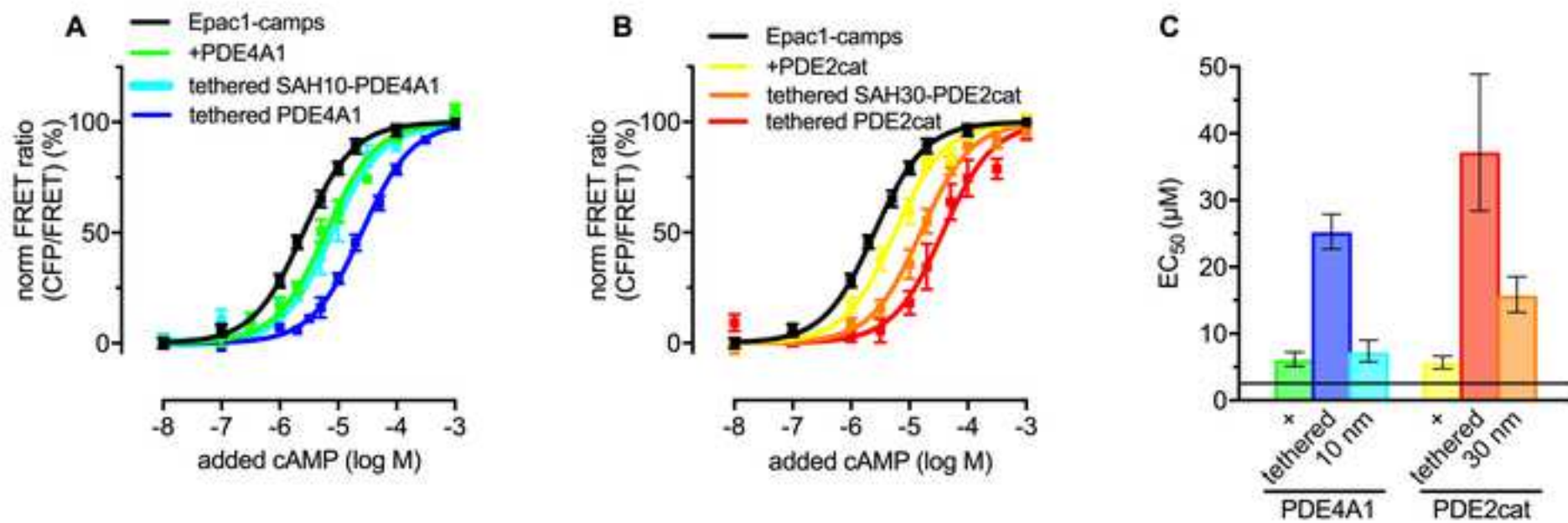


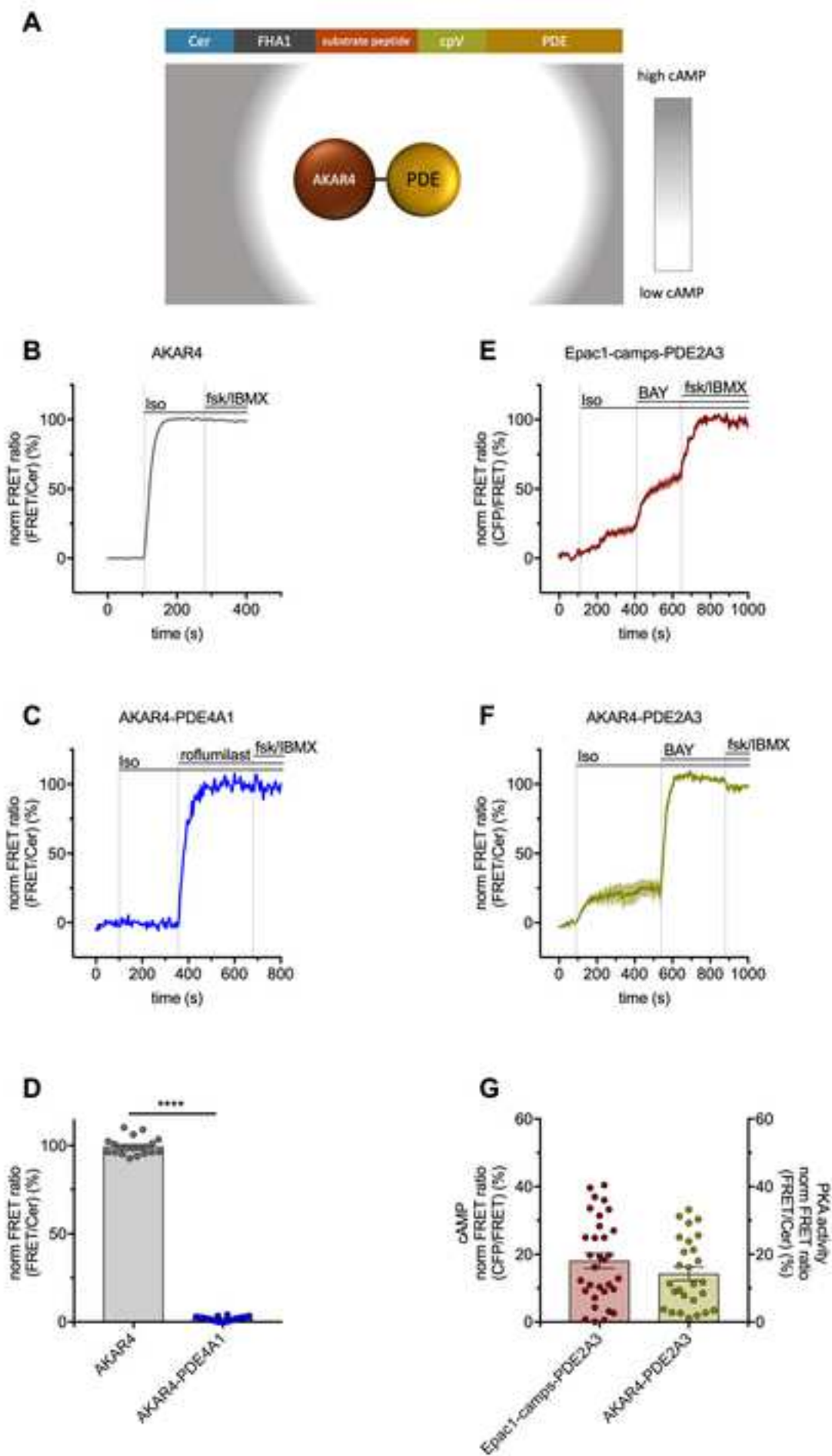












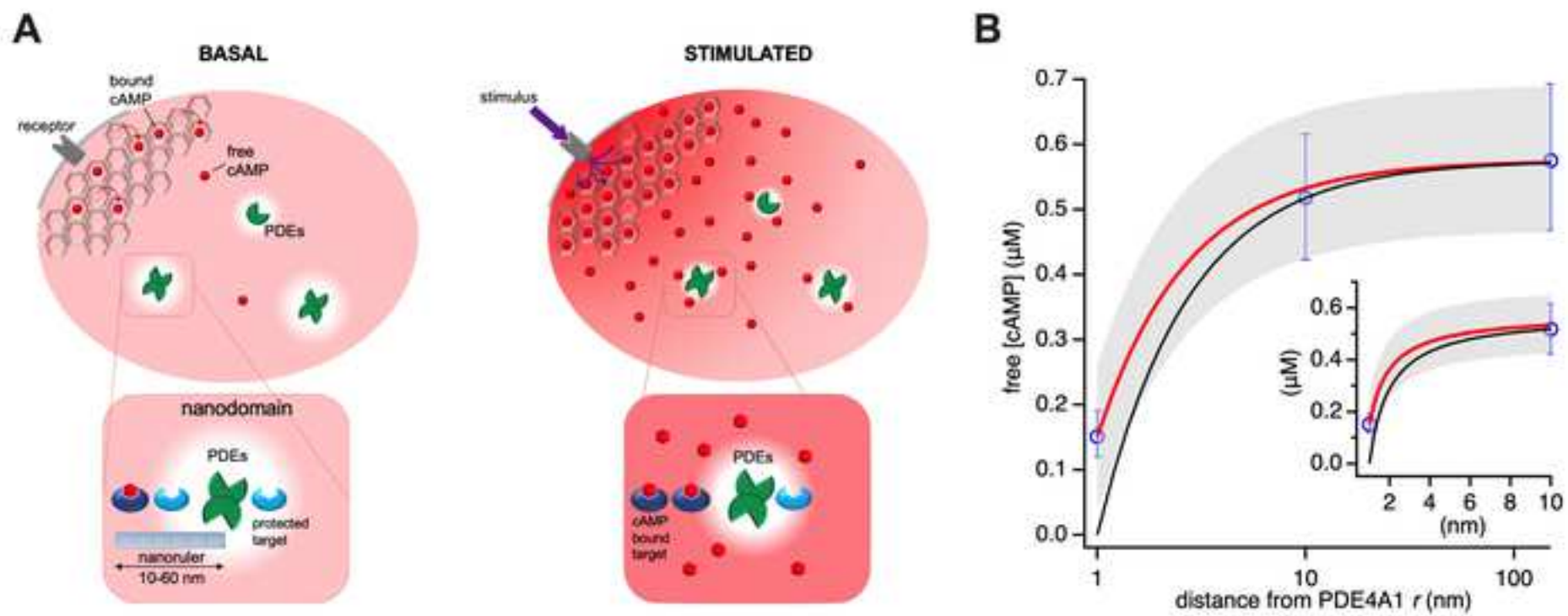


**Table S1. cAMP diffusion coefficients (in  $\mu\text{m}^2/\text{s}$ ) in living cells reported in the literature,****Related to Figures 1 and 2.**

<b>D</b>	<b>Technique</b>	
5	Raster Image Correlation Spectroscopy, fluorescently labeled cAMP (Pharos450-cAMP)	Agarwal et al., 2016
10	Raster Image Correlation Spectroscopy, fluorescently labeled cAMP (Pharos450-cAMP)	Agarwal et al., 2016
32	FRET H187, stimulation with microfluidic device, consideration of PDE activity	Richards et al., 2016
136	FRET HCN2-camps, stimulation with patch pipette, isoprenaline	Nikolaev et al., 2006
270	CNG channel currents, injection of cAMP with a patch pipette	Chen et al., 1999
330	cAMP activated sodium current/injection of cAMP with a patch pipette	Huang et al., 1993
487	FRET Epac1-camps, stimulation with patch pipette, isoprenaline	Nikolaev et al., 2004
780	FRET PKA dissociation, microinjection of cAMP	Bacskai et al., 1993

**Table S2. Oligonucleotides used for biosensor construction, Related to STAR Methods.**

<b>Primer number</b>	<b>Sequence</b>
#1	AAAAAAGGATCCGGAGAAGAGGAAGAGAAA
#2	AAAAAAGGCGCGCCAGAGCCCTTCTTCTTGCGTTTTTC
#3	AAAAAAGGATCCGGAGAAGAGGAAGAGAAGAAG
#4	AAAAAAGGCGCGCCAGAGCCTCTTTGTTTTCTTTCTGC
#5	AAAAAAGGCGCGCCGGGCAGGCATGCGGCCAC
#6	AAAAAAGCGGCCGCTCACTCAGCATCAAGGCT
#7	AAAAAAGGCGCGCCTCCGACGATGAGTATACCAAATT
#8	CTCACTATAGGGAGACCCAAGCTTTAAGGATCCCATGGTGAGCAAGGG
#9	CACCAAGGGCATGGATCCCTCGATGTTGTGGCGGATCTT
#10	AAGATCCGCCACAACATCGAGGGATCCATGCCCTTGGTG
#11	CCCTTGCTCACCATGGGATCCTTAAAGCTTGGGTCTCCCTATAGTGAG
#12	GGGAGACCCAAGCTTAAGGATCCCATGGTGAGCAAG
#13	GCCGCATGCCTGCCCGCGCGCCTCTCGATGTTGTGGCGGAT
#14	ATCCGCCACAACATCGAGAGGCGCGCCGGGCAGGCATGCGGC
#15	CTTGCTCACCATGGGATCCTTAAAGCTTGGGTCTCCCTAT
#16	GACGAGCTGTACAAGTGAGGATCCGCCCTCTCCCTCCCCCCCCCTA
#17	GCAGAAGAAATCCACCAAGGGCATTGTGGCCATATTATCATCGTGTTT
#18	AAACACGATGATAATATGGCCACAATGCCCTTGGTGGATTTCTTCTGC
#19	TAGGGGGGGGGGAGGGAGAGGGGCGGATCCTCACTTGTACAGCTCGTC
#20	GACGAGCTGTACAAGTGAGGATCCAGGCGCGCCGCCCTCTCCCTCCCCCCCCCTA
#21	AAGTTTGGTATACTCATCGTCGGACATTGTGGCCATATTATCATCGTGTTT
#22	AAACACGATGATAATATGGCCACAATGTCCGACGATGAGTATACCAAATT
#23	TAGGGGGGGGGGAGGGAGAGGGGCGGCGCGCCTGGATCCTCACTTGTACAGCTCGTC

## **Methods S1. Synthesis and characterization of the novel fluorogenic cAMP analogue 8-FDA-cAMP, Related to Figures 1 and 2 and STAR Methods.**

### **1) Synthesis and characterization of 8-FDA-cAMP**

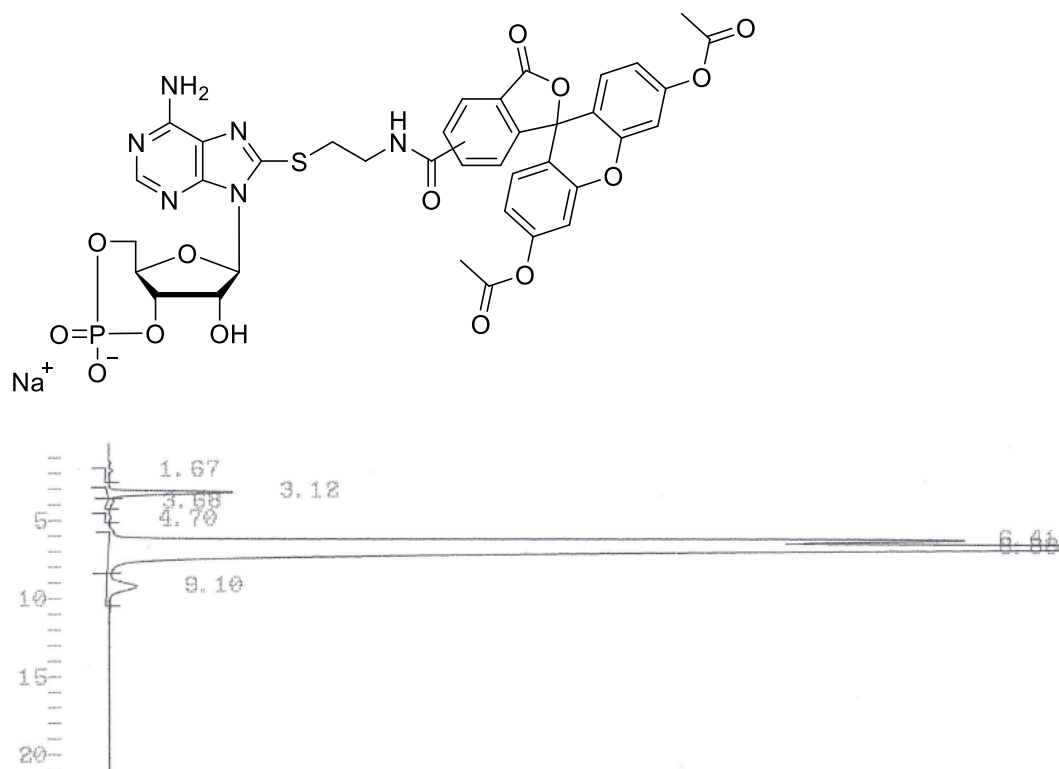
The designed fluorogenic cAMP analog *8-(2-(5(6)-carboxyfluoresceindiacetate)-aminoethylthio)adenosine-3',5'-cyclic monophosphate* (abbreviation: 8-FDA-cAMP, **Methods S1 Figure 1**) was custom-synthesized by Biolog Life Science Institute, Bremen, Germany. The synthesis was initiated by the following two compounds: 5-(and 6)-carboxyfluorescein diacetate, succinimidyl ester (CAS: 150347-59-4) and 8-AET-cAMP (Biolog Life Science Institute, Bremen, Germany; Cat-No.: A 141). It should be noted that 5-(and 6)-carboxyfluorescein diacetate, succinimidyl ester is a mixture of two isomeric compounds and only available in this format. This, by definition, results in a mixture of two isomers of 8-FDA-cAMP, as indicated in the structure (**Methods S1, Figure 1a**).

The identity of 8-FDA-cAMP was assessed by mass spectrometry (ESI-MS) on a Bruker Esquire 600 instrument in methanol/water (1:1) and addition of formic acid. ESI-MS (m/z):  $[M + H]^+$  calculated for  $C_{37}H_{31}N_6O_{14}PS$ : 847.14, found: 847.2.  $[M - H]^+$  calculated for  $C_{37}H_{31}N_6O_{14}PS$ : 845.14, found: 845.2.

To assess the purity of 8-FDA-cAMP, HPLC was performed on a Merck/Hitachi device equipped with a L-6200 intelligent pump, a L-4250 UV-VIS detector (wavelength 276 nm) and a D-7500 integrator. The injection volume was 5  $\mu$ l. *Column*: YMC ODS-A 120-11, RP-18; 250 x 4 mm; *Mobile phase*: 32 % acetonitrile, 50 mM  $NaH_2PO_4$ , pH 5, flow 1.5 mL/min, room temperature. The chromatogram is displayed in **Methods S1, Figure 1 bottom**. The peaks at 6.41 and 6.88 minutes correspond to the two isomers of 8-FDA-cAMP. The peak at 3.12 minutes corresponds to the spontaneously de-esterified compound *8-(2-(5(6)-carboxyfluorescein)-aminoethylthio)adenosine-3',5'-cyclic monophosphate* (abbreviation: 8-



F-cAMP). Based on this data, the purity of 8-FDA-cAMP used in our study can be estimated as 95.6 %. We shall further note that 8-F-cAMP is non cell-membrane permeable, hence, any residual fraction of 8-F-cAMP present in the original stock will not enter the cell, and therefore will be removed upon washout in the experiments we reported in **Figure 1**.



Methods S1 Figure 1: Molecular structure of 8-FDA-cAMP and HPLC chromatogram.

## 2) Photophysical and biochemical characterization of 8-F-cAMP

8-FDA-cAMP is cell-permeable and a substrate for cellular esterases which hydrolyze the two ester bonds per molecule, giving rise to the fluorescent cAMP analogue 8-F-cAMP in intact cells (**Figures 1 and S2**) and cytosolic preparations (**Figure 2**).

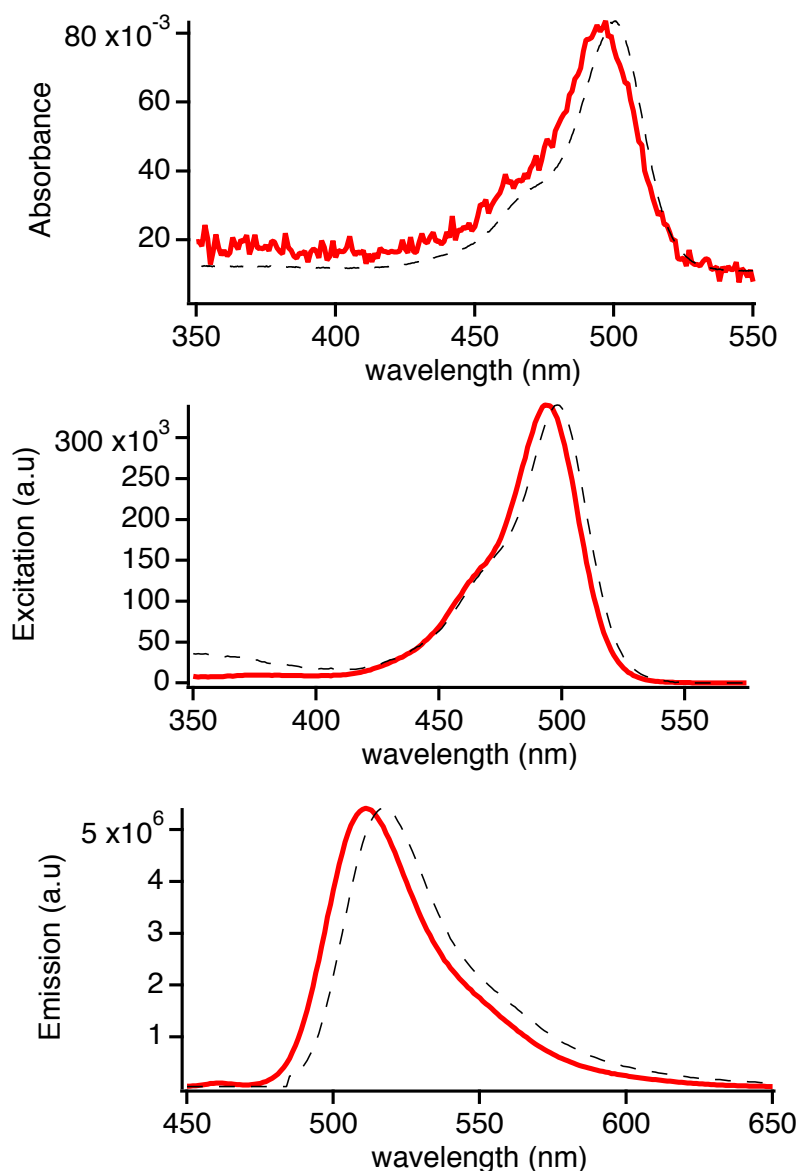
We provide here a photophysical and biochemical characterization of 8-F-cAMP. Based on four lines of experimental evidence we show the absorption, excitation, and emission spectra of 8-F-cAMP, binding of 8-F-cAMP to purified PKA regulatory subunit I alpha (PKA-R1 $\alpha$ ),

activation of endogenous PKA holoenzymes in lysates of HEK293 cells, and the stability towards hydrolysis of 8-F-cAMP by PDEs, using a purified PDE from bovine brain.

For all *in vitro* experiments described below, we used the de-esterified, fluorescent version of 8-FDA-cAMP, i.e. 8-F-cAMP. To generate 8-F-cAMP *in vitro*, a stock solution of 8-FDA-cAMP was diluted in 50 mM TRIS (pH8) and incubated at 30°C for 48 h. This leads to quantitative hydrolysis of the ester bonds as verified by absorption spectroscopy.

### **3) Photophysical characteristics of 8-F-cAMP**

Absorbance, excitation, and emission spectra of 1  $\mu$ M 8-F-cAMP were measured on an Evolution 350 UV/Vis Spectrophotometer (ThermoFisher Scientific, Waltham, MA, USA), using a 50  $\mu$ L volume quartz cuvette (Hellma).

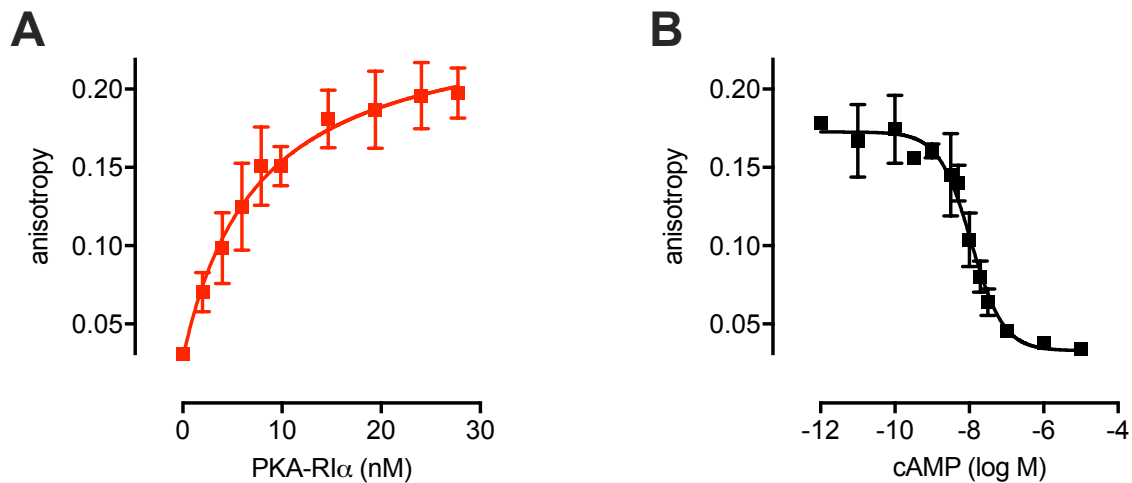


**Methods S1 Figure 2: Photophysical characteristics of 8-F-cAMP.** Absorbance, excitation and emission spectra of 1  $\mu\text{M}$  8-F-cAMP diluted in 50 mM TRIS pH8. The measured extinction coefficient is 80,000  $\text{M}^{-1}\text{cm}^{-1}$  approximately 90% of that of pure fluorescein at comparable pH. The profile of absorption, excitation and emission spectra agrees with that of fluorescein itself which is shown as dashed lines (fluorescein in water at pH 9).

#### 4) Affinities of 8-F-cAMP and cAMP to purified PKA-R1 $\alpha$

All binding assays were done by steady-state anisotropy, where binding is monitored by decreases in anisotropy of the bound *vs.* the free 8-F-cAMP. Purified PKA-R1 $\alpha$  was obtained from Biaffin GmbH & Co KG (Kassel, Germany) and reconstituted in PKA binding buffer

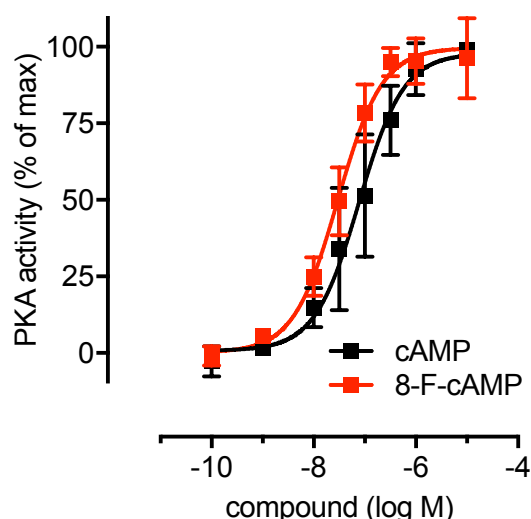
(20 mM MOPS (pH 7) (Sigma-Aldrich Chemie GmbH, Steinheim, Germany), 150 mM NaCl (Carl Roth GmbH & Co. KG, Karlsruhe, Germany), 0.005 % CHAPS (Avanti Polar Lipids, Inc, Alabaster, AL, USA)). Saturation binding experiments were conducted in PKA binding buffer using 3 nM 8-F-cAMP as tracer and increasing concentrations of purified PKA-R1 $\alpha$ . Samples were incubated for 4 min at room temperature and steady-state anisotropy was measured (**STAR Methods**). For competition binding experiments 3 nM 8-F-cAMP was preincubated with increasing concentrations of cAMP in PKA binding buffer. After determining the basal steady-state anisotropy for every single cAMP/8-F-cAMP mixture (i.e. anisotropy of free 8-F-cAMP), 6 nM purified PKA-R1 $\alpha$  was added, incubated for 4 min at room temperature and then PKA-bound steady-state anisotropy was measured.



**Methods S1 Figure 3: 8-F-cAMP and cAMP have the same affinity to PKA-R1 $\alpha$ .** (A) Saturation binding of indicated concentrations of purified PKA-R1 $\alpha$  to 3 nM 8-F-cAMP reveals low nanomolar affinity of 8-F-cAMP to PKA-R1 $\alpha$  ( $K_D(8\text{-F-cAMP}) = 7.5$  nM). (B) Heterologous competition binding (cAMP vs 8-F-cAMP) experiments were performed to quantify the affinity of cAMP to purified PKA-R1 $\alpha$ .  $IC_{50}$  values were Cheng-Prusoff corrected to give a cAMP affinity of  $K_D(\text{cAMP}) = 7.8$  nM. Data in (A) and (B) are means  $\pm$  SD from at least three independent experiments.

## 5) Quantification of PKA activity stimulated by 8-F-cAMP and cAMP in cell lysates

To compare the activation characteristics of 8-F-cAMP and cAMP, we measured the activity of endogenous PKA in HEK293 cell lysates using the PKA Colorimetric Activity Kit (ThermoFisher Scientific, Waltham, MA, USA). HEK293 cell lysates were prepared according to manufacturer's instructions. Lysates were stimulated with increasing concentrations of cAMP or 8-F-cAMP in the presence of 0.5 mM IBMX. PKA activity was normalized to the effect induced by the highest cAMP concentration. Data were fitted with a three parameters logistic function to yield activation constants for half maximal PKA activation (**Methods S1 Figure 4**). Our data demonstrate that 8-F-cAMP is a potent and efficacious activator of PKA, with a potency comparable to that of cAMP.

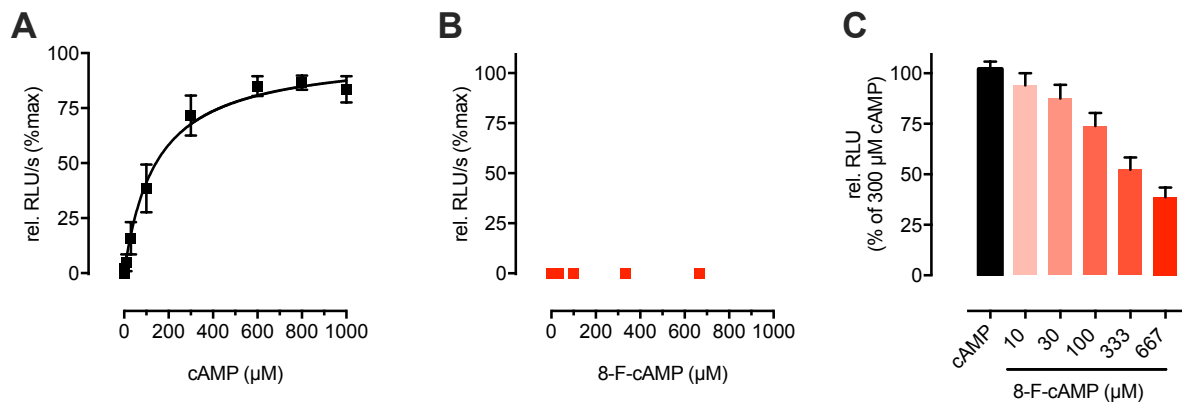


**Methods S1 Figure 4: 8-F-cAMP stimulates PKA activity.** PKA activity was assessed in HEK293 cell lysates in response to increasing concentrations of cAMP and 8-FDA-cAMP in the presence of 0.5 mM IBMX. cAMP (black) and 8-F-cAMP (red) stimulate PKA activity in the nanomolar range:  $EC_{50}(\text{cAMP}) = 77.3 \text{ nM}$ ,  $EC_{50}(\text{8-F-cAMP}) = 29.6 \text{ nM}$ . Data are means  $\pm$  SD from three independent experiments.

## 6) Stability of 8-F-cAMP against hydrolysis by phosphodiesterases

To compare PDE substrate characteristics of cAMP and 8-F-cAMP, we conducted PDE activity assays with purified PDE from bovine brain (PDE1A; P9529 Sigma-Aldrich Chemie

GmbH, Steinheim, Germany). Increasing concentrations of cAMP (mixed with fluorescein (ThermoFisher Scientific, Waltham, MA, USA) at a 1:1 molar ratio) or 8-F-cAMP were added to a mixture of 1 nM PDE and AMP detection reagent (PDELight™, Lonza) in PDE assay buffer (20 mM TRIS, pH 8, 20 mM imidazole (Sigma-Aldrich Chemie GmbH, Steinheim, Germany), 3 mM MgCl<sub>2</sub>, 0.2 mg/mL BSA (Sigma-Aldrich Chemie GmbH, Steinheim, Germany)) at room temperature. Immediately after substrate addition, luminescence was measured every 15 s for 30 min (integration time: 0.1 s) in a plate reader (Neo2, Biotek, Bad Friedrichshall, Germany). The slopes of the initial linear increases in luminescence were plotted against substrate concentrations to give Michaelis-Menten kinetics (**Methods S1 Figure 5**). In contrast to cAMP, 8-F-cAMP is not a PDE substrate up to >600 μM. After completion of kinetic experiments, 300 μM cAMP was added to 8-F-cAMP samples and luminescence was measured again. The resultant inhibition shows that 8-F-cAMP binds to PDE1A but does not serve as a substrate.



**Methods S1 Figure 5: 8-F-cAMP is not a PDE substrate.** (A, B) PDE activity was measured by incubating 1 nM PDE1A with increasing concentrations of cAMP (A) or 8-F-cAMP (B) for 30 minutes. Slopes of linear increases in luminescence (measured as relative light units RLU/s) were normalized to maximal turnover and plotted against substrate concentration to give kinetic profiles. 8-F-cAMP is not a PDE substrate (B). (C) 8-F-cAMP inhibits PDE1A activity. Shown are total luminescence values collected within 30 minutes after addition of 300 μM cAMP. Indicated 8-F-cAMP concentrations were pre-incubated with 1 nM PDE1A for 30 minutes at room temperature. Data are means ± SD of three independent experiments conducted in duplicate.

## Methods S2. Quantitative aspects of cAMP compartmentation at the nanoscale, Related to Figure 7 and STAR Methods.

### 1. Introduction

Our experimental data on diffusion (**Figures 1 and 2**) show that cAMP dynamics are substantially reduced as compared to free diffusion (**Figure 1**). That indicates that cAMP in cells is strongly buffered, which is analogous to what has been observed and modelled for  $\text{Ca}^{2+}$  more than 25 years ago (Wagner and Keizer, 1994). In essence, cAMP is mostly bound to cAMP binding proteins, which are present in cytosol (**Figure 2 and Figure S4**) as well as bound to cellular structures. This *buffering* results in a relatively low concentration of free cAMP, which allows PDEs to create nanometer-sized cAMP gradients where the cAMP concentration at the PDE is decreased to a range which is sufficient to suppress local PKA activation. Here, we would like to delineate some quantitative aspects of cAMP compartmentation at the nanoscale, using the data that we obtained experimentally for PDE4A1.

### 2. cAMP gradients in the vicinity of PDE molecules

At a given cellular concentration of PDEs of  $x$  in units of nM, the average distance between two PDE molecules is at least  $1.186\mu\text{m} / \sqrt[3]{x}$ , which entails  $0.82\ \mu\text{m}$  at 3 nM. We are interested in length scales below 30 nm in this section and therefore consider a single PDE molecule and its vicinity and assume there is no AC molecule close by. This enables us to use the Smoluchowski model representing the catalytic site of the PDE as a diffusing sphere and cAMP as a species diffusing in its vicinity (Rice, 1985, Smoluchowski, 1916). This catalytic site causes the turnover of a given number of cAMP molecules per second, which we denote as the flux  $I$ . We consider stationary states as justified by the duration of measurements. Note that the unbuffered diffusion coefficient for cAMP and not the effective diffusion coefficient enters the

stationary equations on the length scale of a few tens of nm. The PDE enters by the requirement that the total flux of free cAMP towards the PDE at the radius R of the catalytic site equals the turnover I (Rice, 1985)

$$4\pi R^2 D \left. \frac{\partial [\text{cAMP}]}{\partial r} \right|_{r=R} = I.$$

The concentration of free cAMP at a large distance from the PDE molecule is the spatially averaged cAMP concentration called  $[\text{cAMP}]_{\text{bulk}}$ . The stationary solution of the diffusion equation in spherical coordinates with the PDE in the center is

$$[\text{cAMP}](r) = [\text{cAMP}]_{\text{bulk}} - \frac{I}{4\pi D r} \quad (1)$$

with r denoting the radius coordinate. The concentration at the encounter radius  $\sigma$  is

$$[\text{cAMP}](\sigma) = [\text{cAMP}]_{\text{bulk}} - \frac{I}{4\pi D \sigma} \quad (2)$$

The PDE would be a perfect absorber ( $[\text{cAMP}](\sigma)=0$ ) with

$$I \geq 4\pi D \sigma [\text{cAMP}]_{\text{bulk}} = 435 \text{ s}^{-1}, \quad (3)$$

where we used  $\sigma=1$  nm,  $[\text{cAMP}]_{\text{bulk}}=0.575$   $\mu\text{M}$  (Table 1) and  $D=100$   $\mu\text{m}^2\text{s}^{-1}$ .

### 3. *Estimation of the spatial concentration profile around PDE4A1 deduced from FRET experiments in cytosolic preparations and in intact cells*

If the concentration of Epac1-PDE4A1 molecules in cytosolic preparations is not too large, the concentration profile around the individual molecules also obeys the  $(1-1/r)$ -dependency of Eq. (1). Above, we have written the profile in terms of turnover I and the diffusion coefficient D. We can also write it in terms of the radius  $R_0$  where the concentration would be 0, if the profile reached down to  $R_0$ :



$$[\text{cAMP}](r) = [\text{cAMP}]_{\text{bulk}} \left( 1 - \frac{R_0}{r} \right).$$

We denote the distance between the catalytic site of PDE4A1 and the sensor's binding site with  $R_{\text{sens}}$  and obtain for the concentration seen by the sensor

$$[\text{cAMP}](R_{\text{sens}}) = [\text{cAMP}]_{\text{bulk}} \left( 1 - \frac{R_0}{R_{\text{sens}}} \right).$$

The fluorescence we see in cells expressing Epac1-PDE4A1 is

$$F = F_{\text{max}} \frac{[\text{cAMP}]_{\text{bulk}} \left( 1 - \frac{R_0}{R_{\text{sens}}} \right)}{\text{EC}_{50} + [\text{cAMP}]_{\text{bulk}} \left( 1 - \frac{R_0}{R_{\text{sens}}} \right)} = F_{\text{max}} \frac{[\text{cAMP}]_{\text{bulk}}}{\left( 1 - \frac{R_0}{R_{\text{sens}}} \right) + [\text{cAMP}]_{\text{bulk}}} = F_{\text{max}} \frac{[\text{cAMP}]_{\text{bulk}}}{\text{EC}_{50}^{\text{rs}} + [\text{cAMP}]_{\text{bulk}}}$$

$$\text{EC}_{50}^{\text{rs}} = \frac{\text{EC}_{50}}{\left( 1 - \frac{R_0}{R_{\text{sens}}} \right)}, \quad \frac{\text{EC}_{50}}{\text{EC}_{50}^{\text{rs}}} = \left( 1 - \frac{R_0}{R_{\text{sens}}} \right).$$

In intact cells we can write for the concentration *seen* by the sensor

$$[\text{cAMP}](R_{\text{sens}}) = [\text{cAMP}]_{\text{bulk}} \left( 1 - \frac{R_0}{R_{\text{sens}}} \right), \quad \frac{[\text{cAMP}](R_{\text{sens}})}{[\text{cAMP}]_{\text{bulk}}} = \left( 1 - \frac{R_0}{R_{\text{sens}}} \right)$$

Since we measure cAMP concentrations (**Figures 3, 4**) and know the  $\text{EC}_{50}$  values of the sensors for cAMP, we can calculate and compare the values from the data obtained from cytosolic preparations and intact cells. Table 1 lists the intracellular cAMP concentration estimated from

Figure 3. Based on these values, Table 2 lists the estimates for  $1 - \frac{R_0}{R_{\text{sens}}}$ .

Table 1 Ranges for concentrations of free cAMP at the sensor estimated from Figure 3.

	Average ( $\mu\text{M}$ )	Min ( $\mu\text{M}$ )	Max ( $\mu\text{M}$ )
cAMP (Epac1 + PDE4A1)	0.575	0.468	0.692
cAMP (Epac1-PDE4A1 tethered)	0.151	0.120	0.191
cAMP (Epac1-SAH10-PDE4A1):	0.518	0.423	0.616

Table 2 Comparison of concentration ratios in cytosolic preparations and in intact cells using the intracellular concentrations from Table 1.

	$EC_{50}$ ( $\mu\text{M}$ )	$1 - \frac{R_0}{R_{\text{sens}}}$	
		as $\frac{EC_{50}}{EC_{50}^{\text{rs}}}$ in cytosol	as $\frac{[\text{cAMP}](R_{\text{sens}})}{[\text{cAMP}]_{\text{bulk}}}$ in cells
Epac1camps + PDE4A1	6.06	control PDE4A1	
Epac1camps-PDE4A1	25.02	0.242	0.270
Epac1-camps-SAH10-PDE4A1	7.20	0.842	0.901
Epac1-camps + PDE2cat	5.62	control PDE2cat	
Epac1-camps-PDE2cat	37.2	0.151	0.363
Epac1-camps-SAH30-PDE2cat	15.7	0.358	0.363

We conclude

$$\frac{[\text{cAMP}](R_{\text{sens}})}{[\text{cAMP}]_{\text{bulk}}} \approx \frac{EC_{50}}{EC_{50}^{\text{rs}}} = 1 - \frac{R_0}{R_{\text{sens}}}.$$

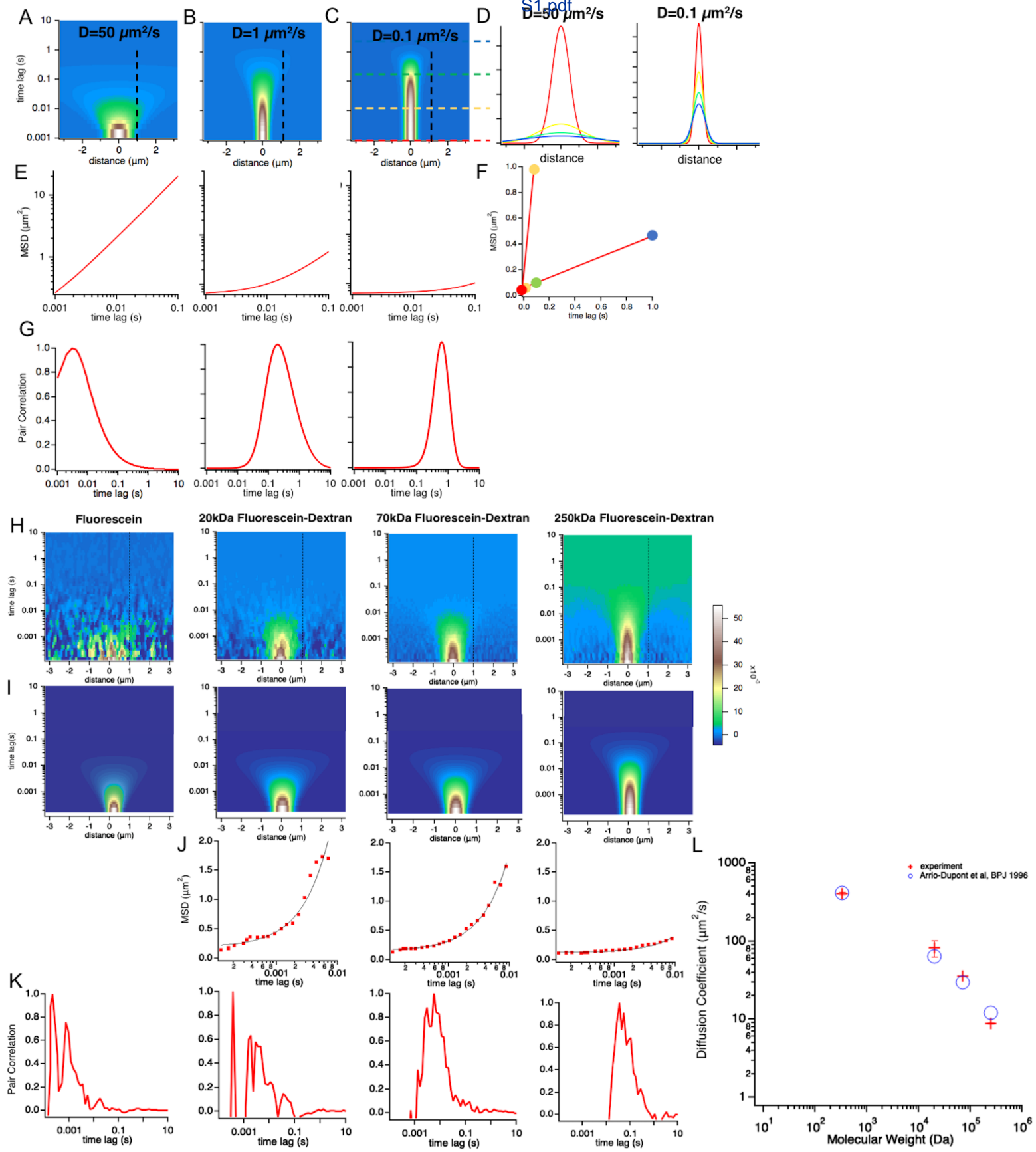
The ratio of bulk concentration to local concentration at PDE4A1 dimers in cytosolic preparations is very similar to the values in intact cells.

We obtain from Eq. (2)

$$I = 4\pi D\sigma([\text{cAMP}]_{\text{bulk}} - [\text{cAMP}](\sigma)).$$

Taking the concentrations at the sensor as estimates for  $[\text{cAMP}](\sigma)$  and with  $D=100 \mu\text{m}^2\text{s}^{-1}$ ,  $\sigma=1 \text{ nm}$ ,  $[\text{cAMP}]_{\text{bulk}}=0.575 \mu\text{M}$  and  $[\text{cAMP}](\sigma)=0.151 \mu\text{M}$  (Table 1) we obtain  $I=320 \text{ s}^{-1}$ , i.e.  $160 \text{ s}^{-1}$  per PDE4A1 monomer, given that we find PDE4A1 in cells predominantly as dimers. With the values in the Min and Max columns of Table 1 we obtain  $263 \text{ s}^{-1}$  and  $379 \text{ s}^{-1}$ , respectively, as dimer turnover rates.

Based on our FRET data in **Figure 3**, we can estimate the catalytic activity of PDE4A1 in intact cells. PDE4A1 activity compensates for isoproterenol-induced cAMP production in the stationary state. The rise of  $[\text{cAMP}]$  upon PDE4A1 inhibition (with roflumilast) approximately equals the rate of cAMP degradation before inhibition. We have determined the rate of the increase in free  $[\text{cAMP}]$  upon inhibition of PDE4A1 tethered to Epac1-camps (**Figure 3E**) with roflumilast to be in the range of  $1 \mu\text{M}/\text{s}$ . We also estimated the concentration of buffering sites B in cells to be in the range of  $7.5\text{-}30 \mu\text{M}$  (**Figure S4**), with a dissociation constant  $K_B$  of  $0.1\text{-}0.5 \mu\text{M}$ . Our estimate of the PDE4A1 dimer concentration is  $30\text{-}100 \text{ nM}$  (**Figure S7**). In line with the above estimate for the PDE4A1 dimer turnover based on the Smoluchowski model, we obtain here also  $320 \text{ s}^{-1}$  with  $B = 20 \mu\text{M}$ ,  $K_B = 0.5 \mu\text{M}$  and  $30 \text{ nM}$  PDE4A1.



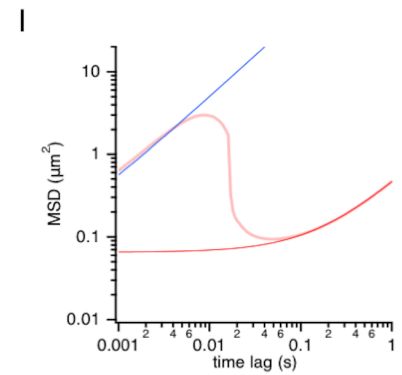
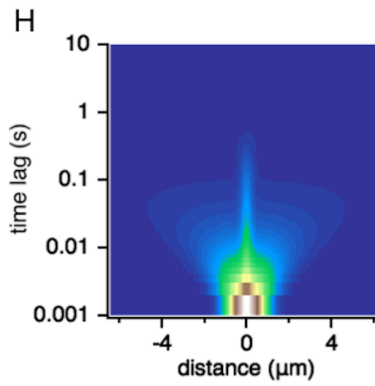
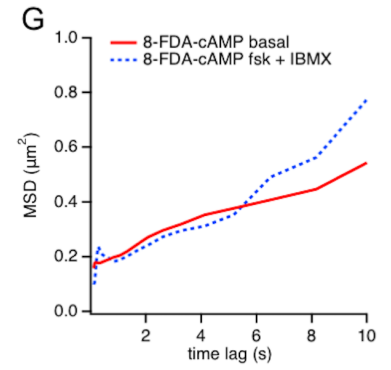
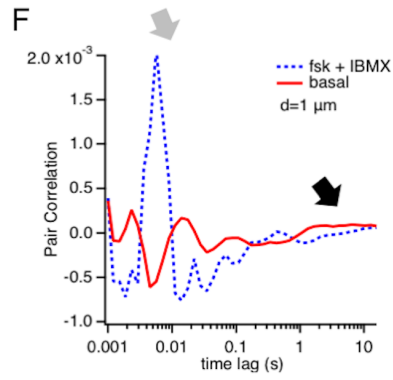
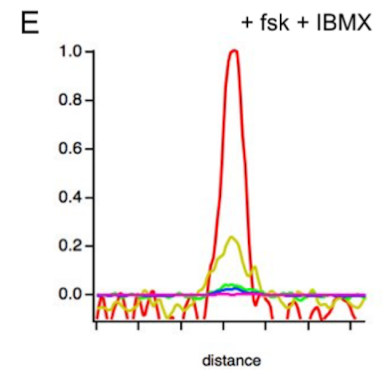
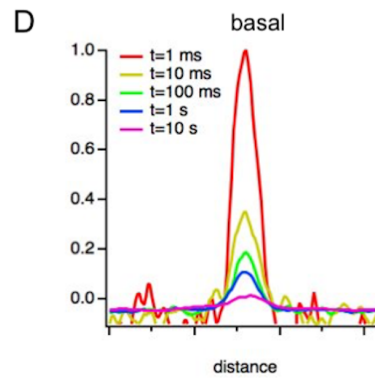
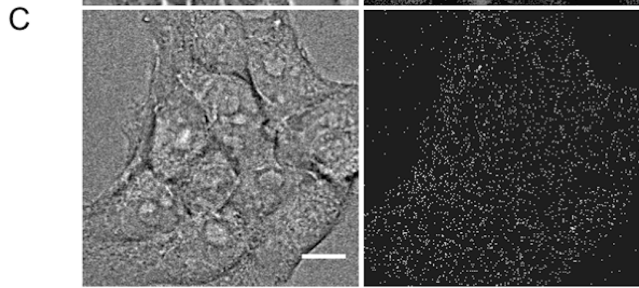
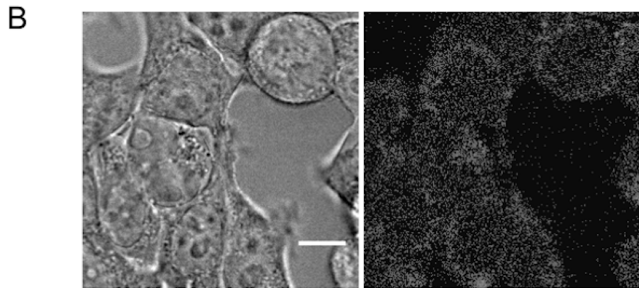
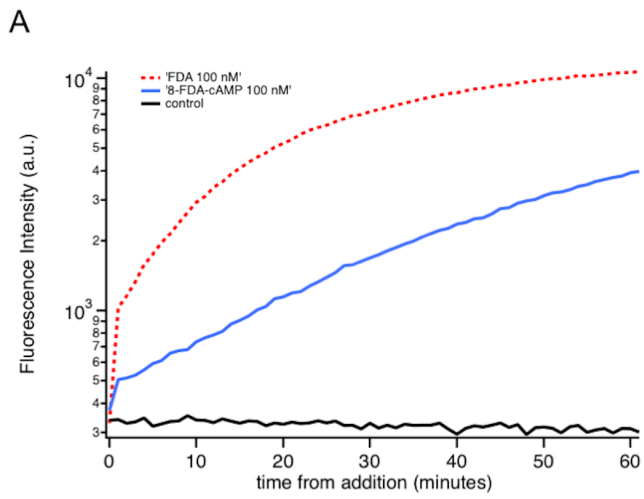
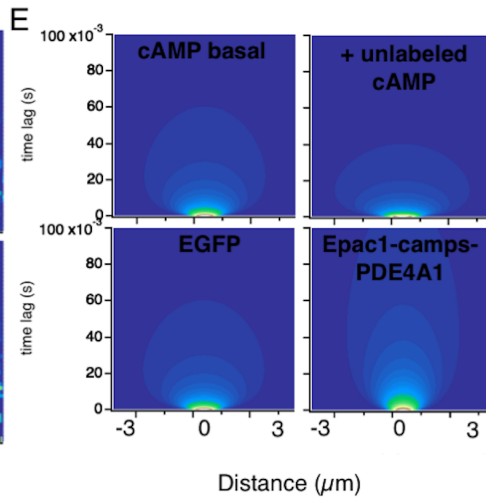
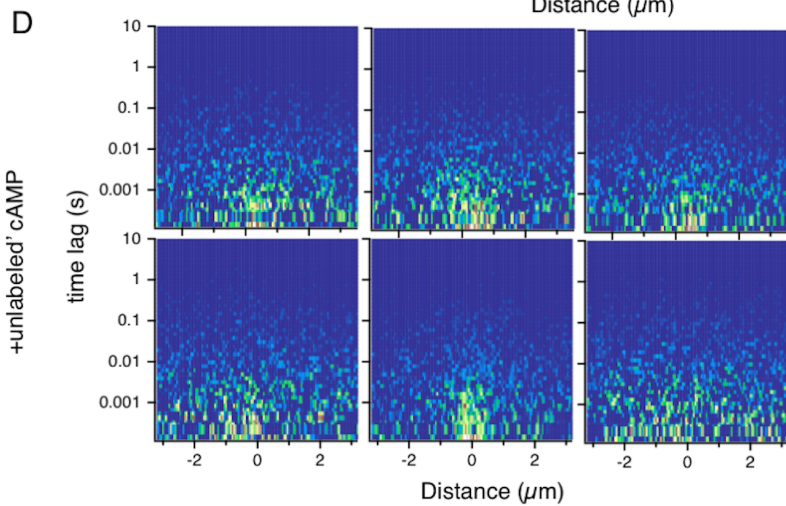
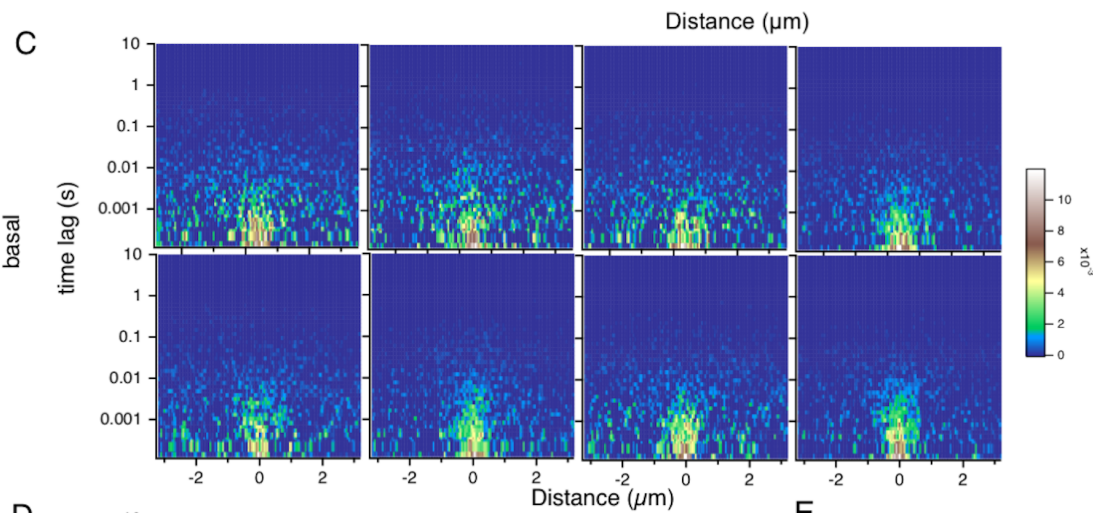
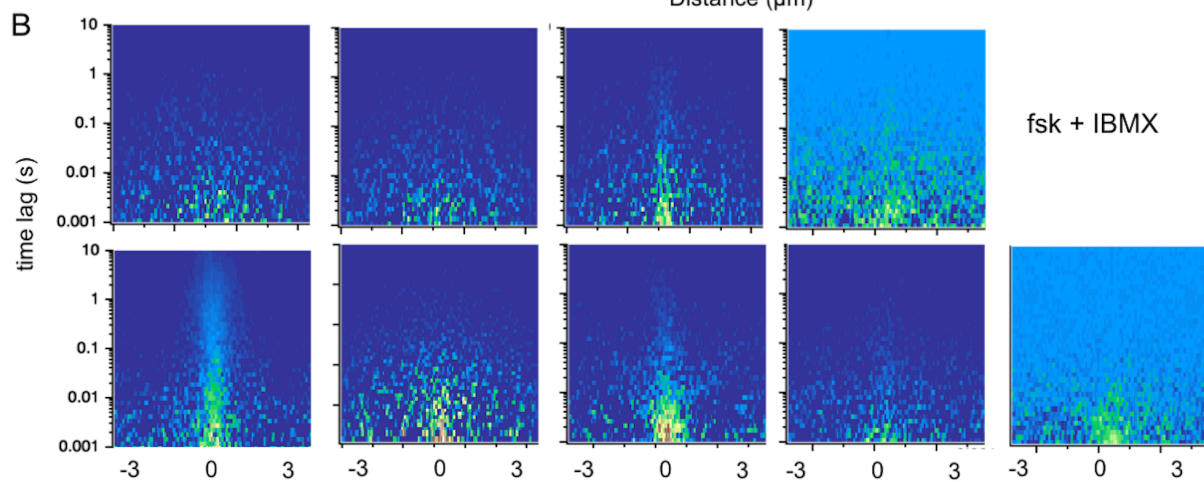
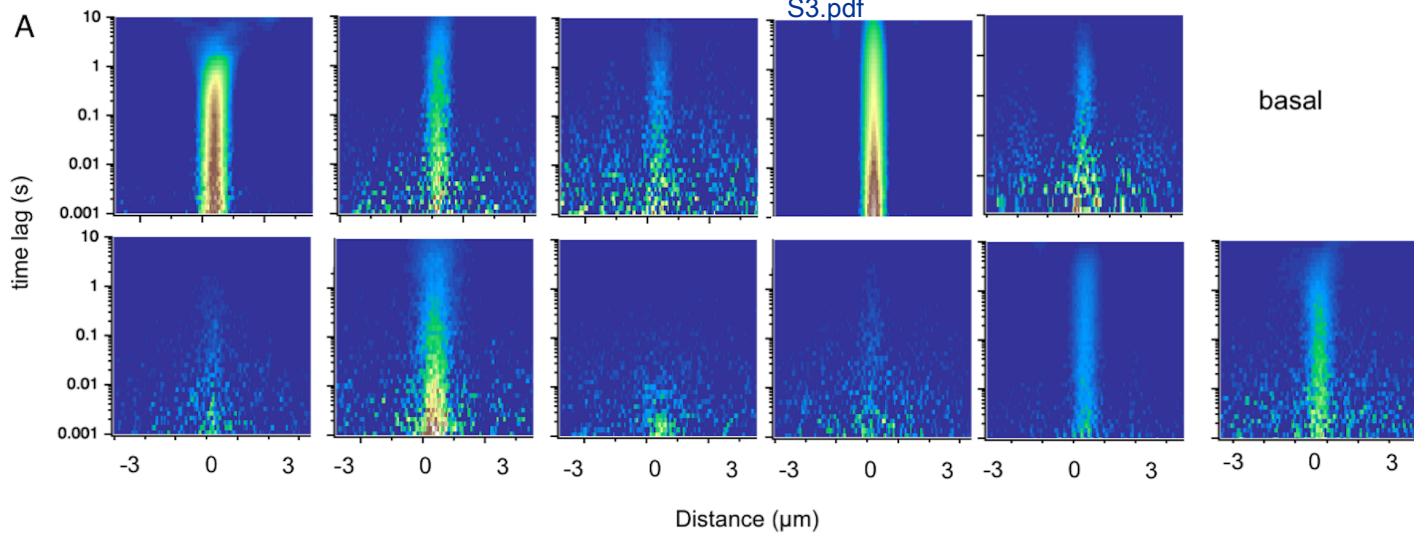
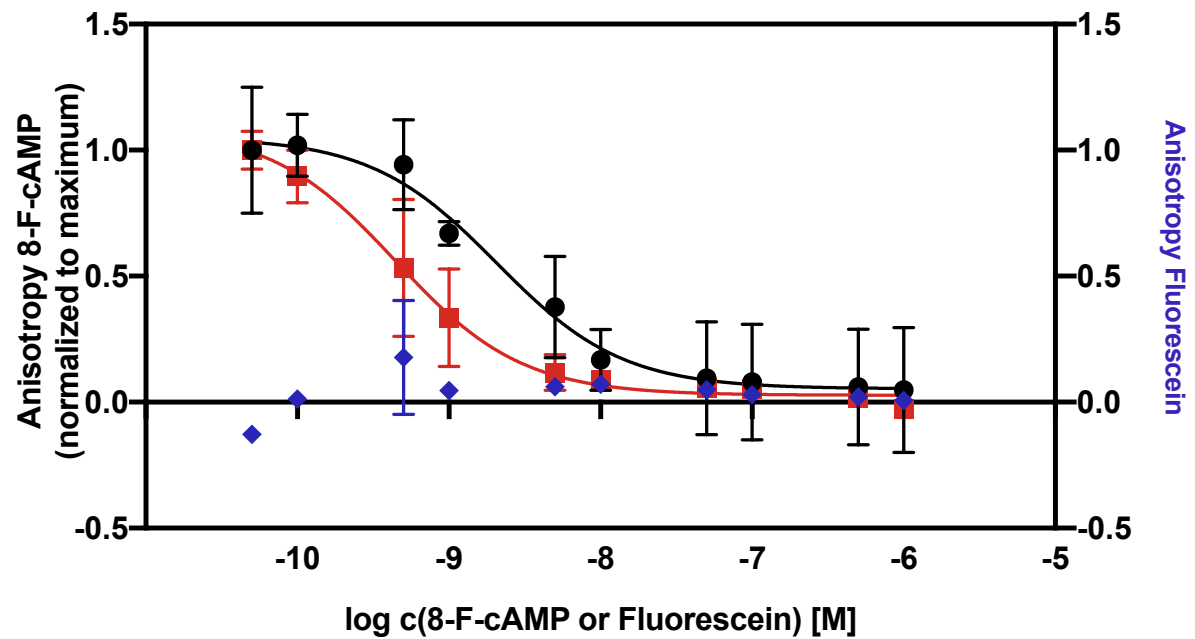


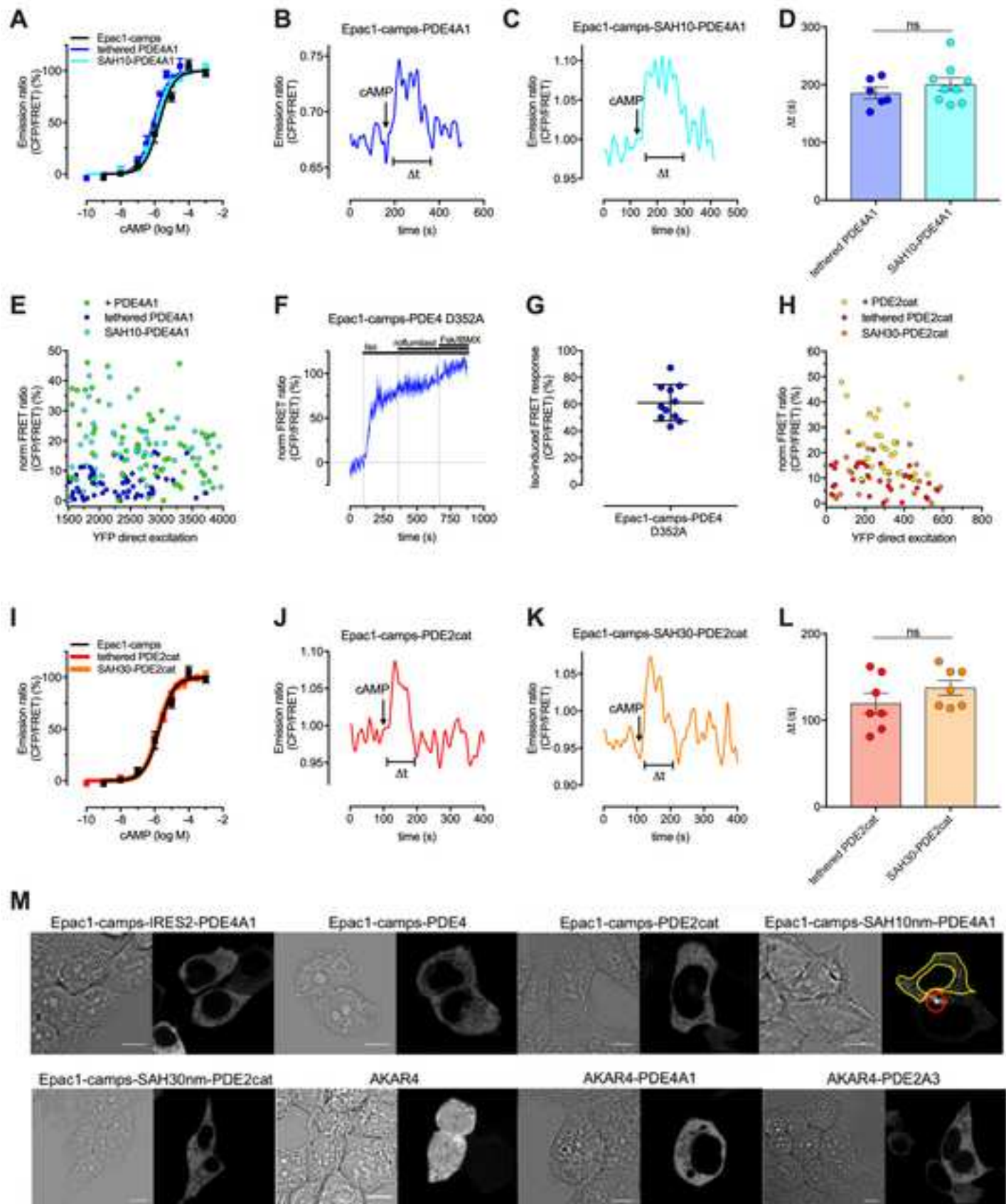
Figure S3

Click here to access/download;Supplemental Figure;Figure S3.pdf

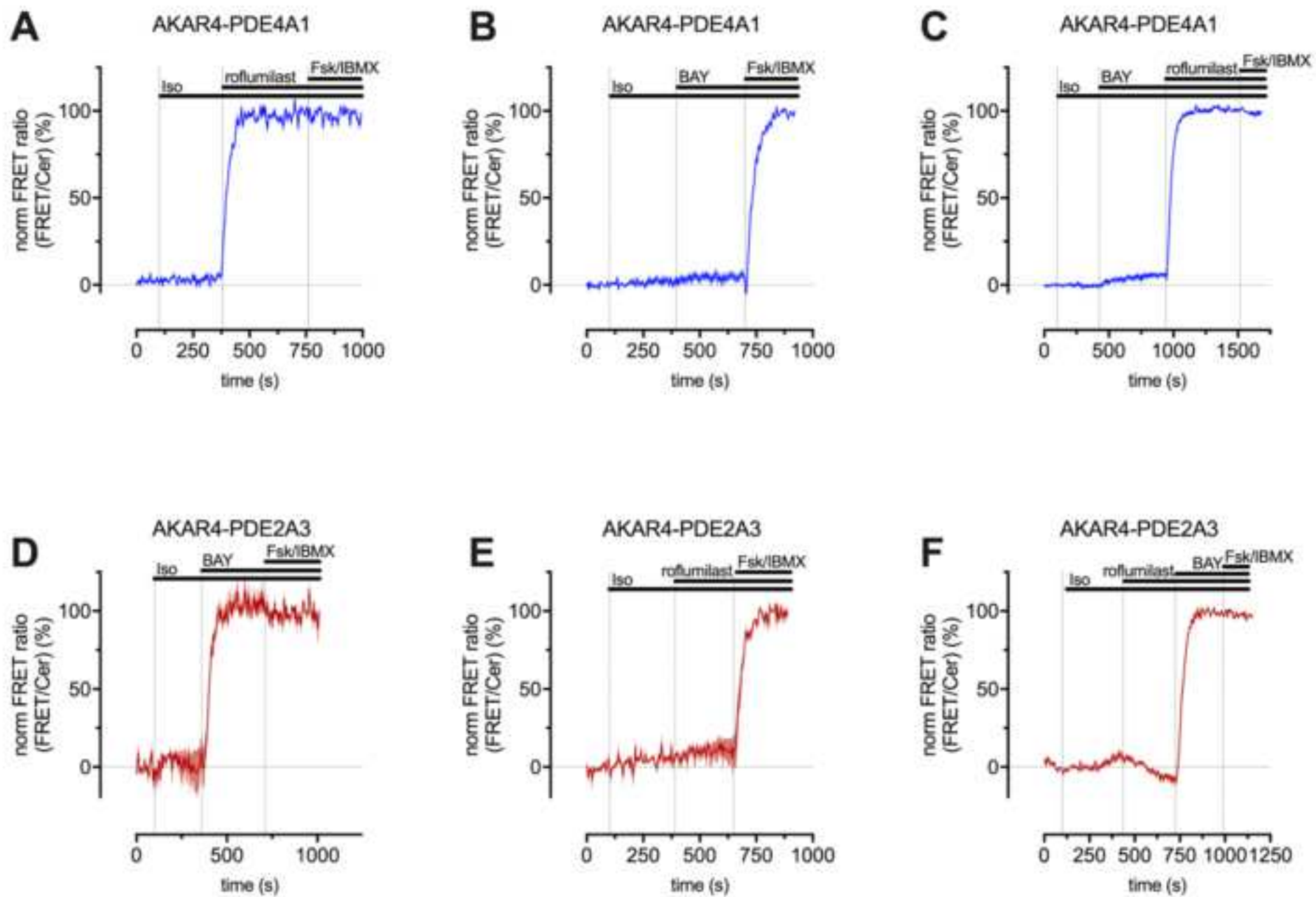




- 60x diluted cytosol 8-F-cAMP
- 1500x diluted cytosol 8-F-cAMP
- ◆ 60x diluted cytosol Fluorescein







**Molecular Brightness (counts/molecule/s)**

● Epac1-camps-  
IRES2-PDE4A1

■ Epac1-camps-PDE4A1

15000

10000

5000

0

